

# Forecasting Buoy Observations Using Physics-Informed Neural Networks

Austin Schmidt\*, Pujan Pokhrel<sup>†</sup>, Mahdi Abdelguerfi<sup>‡</sup>,  
Elias Ioup<sup>§</sup>, and David Dobson<sup>¶</sup>

Canizaro Livingston Gulf States Center for Environmental Informatics<sup>\*†‡</sup>

University of New Orleans

New Orleans, Louisiana 70148

Email: {\*aschmid2, †ppokhre1, ‡mahdi}@uno.edu

Center for Geospatial Sciences Naval Research Laboratory<sup>§¶</sup>

Stennis Space Center, Mississippi 39529

Email: {§elias.ioup, ¶david.dobson}@nrlssc.navy.mil

## Abstract

Methodologies inspired by physics-informed neural networks (PINNs) were used to forecast observations recorded by stationary ocean buoys. We combined buoy observations with numerical models to train surrogate deep learning networks that performed better than with either data alone. Numerical model outputs were collected from two sources for training and regularization: HYCOM and ERA5. A hyperparameter determines the ratio of observational and modeled data to be used in the training procedure, so we conducted a grid search to find the most performant ratio. Overall, the technique improved the general forecast performance compared to non-regularized models. Under specific circumstances, the regularization mechanism enabled the PINN models to be more accurate than the numerical models. This demonstrates the utility of combining various climate models and sensor observations to improve surrogate modeling.

## Index Terms

PINN, Deep Learning, HYCOM, ERA5, Recurrent Model, Surrogate Model

## I. INTRODUCTION

25  
26  
27  
28  
29  
30  
31  
32  
33  
34  
35  
36  
37  
38  
39  
40  
41  
42  
43  
44  
45  
46  
47  
48  
49  
50  
51  
52  
53  
54  
55

OCEAN parameter forecasting is studied for various applications, like climate modeling, marine life population surveying, and water quality monitoring. There is a clear need across industries to have fast and far-reaching forecasts. As such, research and improvements in ocean and climate modeling tools have continued to be interesting and necessary in literature. Well-studied numerical solutions for this task include Navier-Stokes and advection-diffusion, which are formulated as sets of partial differential equations (PDEs) for modeling flow systems. Building primitive equations into a more complex model yields global ocean and climate models for accurate, full-coverage simulations [1] [2] [3]. The initial values and boundary conditions of the modeled system are important for accurately modeling physical behaviors in this way [4]. Initial values are recorded as sparse observations across the world's oceans using different methods. These methods include free-floating buoys that record data by following ocean currents, stationary buoys for monitoring fixed locations, and satellites for collecting global imagery [5]. As the viability of the modeled forecasts greatly depends on accurate estimations of the initial values, data assimilative systems have been a point of research, and assimilating observations with numerical models has shown improved results [6]. In the case of the United States Navy, researchers have developed the global coupled atmosphere-ocean-sea ice forecasting system called the Navy Earth System Prediction Capability (Navy-ESPC) where modeled data is assimilated with observations for an improved result [7]. However, observations can be missing such that there is no data availability. In this situation, the data assimilation scheme cannot be taken advantage of. Therefore, there exists some motivation to generate discrete observation forecasts for their integration into an assimilation pipeline. To this end, we investigate a generalized procedure to predict sparse ocean observation values.

Surrogate deep learning models are trained using available historical data to model a system given prior input values. The main benefit of this technique is that forecasts are generated more quickly than when evolving a numerical model. Recurrent network architectures like long short-term memory (LSTM) networks and Transformers are used to propagate information forward when making long-term predictions, making them popular choices for modeling ocean parameters as surrogate models [5]. When surrogate modeling ocean parameters, data is required from recorded observations, numerical model outputs, or both. In this work, we take particular interest in two data assimilated numerical models which provide training and regularization data. The

56 Hybrid Circulation Ocean Model (HYCOM) is a hybrid isopycnic model which sees improvement  
57 over its predecessor in shallow water and unstratified ocean regions. [1]. ERA5 is the fifth  
58 reanalysis experiment of the European Centre for Medium-Range Weather Forecasts (ECMWF)  
59 model for global climate and weather features. [2].

60 By combining the numerical models with buoy-collected observation data, we show how a  
61 physics-regularized approach can be used to improve observation forecasting. Thus, we consider  
62 physics-informed neural networks (PINNs) for approximating numerical models to accurately  
63 forecast a single discrete point (i.e., an observation). A PINN is a neural network which is  
64 regularized at training time by applying penalties in the loss function. The penalties are scored  
65 by comparing adherence to a PDE-based numerical model [4]. We investigate if the forecasting  
66 result of real-world sensor data collected by stationary ocean buoys can be more accurately  
67 forecasted when regularized by the prior mentioned numerical models. Since reanalysis data  
68 exists for many ocean and climate features, we use the high-quality numerical model outputs to  
69 regularize our PINN model.

70 As far as we know, we are the first to integrate HYCOM and ERA5 data as a regularizing  
71 source in a PINN-inspired network. We show that the physical models may be used with  
72 recorded buoy data to provide more stable long-term predictions due to the regularization support.  
73 Our methodology differs from other PINN research by modeling only observations and, more  
74 importantly, by the way in which we implement the loss function. These differences will be  
75 discussed further in the upcoming Related Works section. To assess our models, sea surface  
76 temperature (SST), gust strength, and air pressure are sparsely forecasted using our technique.  
77 The main contributions of this paper are as follows. We train deep learning models to recursively  
78 forecast physical parameters as recorded by free-floating ocean buoys. We define a custom  
79 loss function to use numerically modeled data and observation data as sources for training  
80 physics regularized models. The methodology is capable of handling situations where a physical  
81 parameter is available from both sources or a single source. When both sources of data are  
82 available for a feature, we show how the surrogate may be trained using a ratio of the training  
83 errors from each source. The most performant surrogate for the test data is found through a grid  
84 search of the static regularization term,  $\lambda$ , which controls the ratio of errors. We demonstrate  
85 the flexibility of PINNs to combine different numerical models using a surrogate deep learning  
86 model, which outperforms the non-regularized deep learning models. We discuss the numerical  
87 models and their effect on the rolling forecast ability of our surrogate model for up to 24 hours.

88 The rest of this paper is formatted as follows: II. Related Works; III. Methods; IV. Results; and  
89 V. Conclusions.

## 90 II. RELATED WORKS

91 Ocean surrogate models have been advancing with the advent of deep learning, and more  
92 refined machine learning approaches [5][8]. Research into deep learning surrogate modeling of  
93 SST shows promising results as SST can be forecasted as discrete points [9], as a field [10], or  
94 as a super-resolution field [11]. Instead of directly solving intractable formulations like Navier-  
95 Stokes or other prognostic equations for ocean modeling, a data-driven surrogate model is trained  
96 using the substantial amounts of historical training data available via numerical models or raw  
97 observations [12]. The use of observation assimilated models to train deep learning surrogates  
98 has been seen multiple times using both HYCOM [13][14] and ERA5 [15][16][17] models.  
99 Through back propagation a deep learning model learns a parameterized representation of the  
100 underlying physical phenomenon which are otherwise modeled numerically. Surrogate models  
101 may be preferred over traditional models due to faster outputs once the model has been trained  
102 [8]. For example, in [18], approaching hurricane parameters are forecasted in seconds. Machine  
103 learning surrogate models will generally have more numerical instability when compared to  
104 numerical models in forecasting experiments. This speed and accuracy trade-off is seen in  
105 the conclusions of surrogate modelling studies for data assimilation in dynamic subsurface  
106 flow [12] and regional wind/wave forecasting [19]. In both papers, the forecast accuracy was  
107 similar or lower than numerical models, but the computational speed was greatly improved.  
108 One keynote on numerical stability and model accuracy is that the generalization of machine  
109 learning surrogate modeling is not assured for all cases. Authors observe the stability difference  
110 in operational planning with dynamic constraints where the forecasting stability is very good for  
111 some deep learning surrogate models but unstable when using other machine learning techniques  
112 [20]. This forecasting stability problem is also considered in [21] where outputs of physics-  
113 based numerical models are combined and used as supervised learning training sets to promote  
114 more accurate forecasts than when used independently. Furthermore, the surrogate modeling  
115 task can be used with data assimilation to correct numerical model error in an online fashion  
116 [22]. As such, surrogate models have a place among the more carefully calculated simulation-  
117 based numerical models, like HYCOM and ERA5. This is especially true in applications where

118 numerical solutions are too complex or computationally intensive for real time analysis and the  
119 acceptable error threshold is high.

120 Physics-informed neural networks are referred to as such because they leverage physical  
121 constraints within the model's loss function during training to enforce convergence to governing  
122 physical laws. This type of network was popularized in the deep learning community by Raissi  
123 et al. in 2017 and 2019 [23]. The introduction of differential equations that define physical phe-  
124 nomenon to the training procedure is found to improve the model's resilience to noise [24]. PINNs  
125 are regularized in training by comparing model performance to the adherence of the introduced  
126 PDEs while also fitting data points to unique solutions [25]. The result of these forecasting  
127 models is that we can incorporate noisy data into existing algorithms, ignore complex mesh  
128 generation, and tackle high-dimensional problems governed by parameterized PDEs. Originally,  
129 research has focused on surrogate modeling with PINNs for solving systems governed by the  
130 Burgers' and Navier-Stokes equations [26]. PINNs have recently been investigated in industry  
131 informatics settings such as modeling flow equations for ocean models [24], modeling crack  
132 propagation [27][28], modeling leakage [29], modeling faults [30], and modeling electric loads  
133 [31]. Forecasting SST is commonly found as a full-coverage modeling problem combining either  
134 generative models [32][33] or convolutional neural networks [34] with various PDEs. Continual  
135 discussion on PINNs and the types of equations usually solved can be reviewed in [4] and [35].

136 We have not seen any other works that use a ratio of numerical model data and observations to  
137 train and regularize a deep neural network for surrogate modeling. Our methods share similarities  
138 with [21], who utilizes numerical models as training data for surrogate models. However, we  
139 employ our PINN-inspired approach to regularize models by combining both observations and  
140 numerical outputs. Furthermore, our work differs methodologically from the prior mentioned  
141 PINN research in two significant ways. First, there is no differentiation or simulation step to solve  
142 selected PDEs within the surrogate training procedure. This is the case because the numerical  
143 model pipeline is too computationally intensive for this to be feasible. Instead, the selected  
144 climate and oceanography models, HYCOM and ERA5, have already undergone comprehensive  
145 modeling and data assimilation processes which provide high quality, historical simulation data.  
146 Using the pre-computed data instead of directly solving PDEs means the numerical model can be  
147 arbitrarily complex and we do not need to implement the formulation for use in our framework.  
148 The second divergence is the role of the hyperparameter  $\lambda$  within the PINN loss function. The  
149 traditional PINN training loss function sums the performance of the surrogate model and the

150 divergence when compared to the numerical solution of selected PDEs. In that case,  $\lambda$  is used  
151 as the multiplicative weighting term to determine how much of a contribution the divergence  
152 from the numerical solution has on the final loss output. Instead, we use  $\lambda$  as a mechanism  
153 to control a weighted ratio of observation versus modeled data in training. This ratio of loss  
154 from multiple sources improves the training process when numerical data, observational data, or  
155 both are noisy. The proposed buoy forecasting task is inspired by [36], but we forecast multiple  
156 buoy parameters, test additional numerical models (ERA5 and HYCOM), and apply our physics-  
157 regularized training methodology, as main differences. So, we show, in an experimental approach,  
158 that we may use complex solutions calculated by numerical climatology and ocean flow models  
159 as a means of regularizing surrogate PINN models. We aim to demonstrate that a PINN can  
160 internalize the simulated outputs of ocean and climate models to be more capable of forecasting  
161 unseen buoy values.

### 162 III. METHODS

163 In this section, we discuss the methodologies utilized in investigating our PINN-inspired  
164 surrogate models. The models are trained to forecast ocean observations at fixed locations given  
165 prior conditions. The numerical models, HYCOM and ERA5, regularize the model at training  
166 time and offer additional input features. The section is organized as follows: A. Numerical  
167 Models Overview; B. Data and Feature Processing; C. Deep Learning Models; and D. Metrics  
168 and Testing Strategy.

#### 169 A. Numerical Models Overview

170 The Hybrid Circulation Ocean Model (HYCOM) system is a primitive equation model for  
171 general ocean circulation that evolved from the Miami Isopycnic-Coordinate Ocean Model  
172 (MICOM) system developed by Rainer Bleck and associates [1] [3]. HYCOM, like MICOM,  
173 is a primitive-equation model containing five prognostic equations. Two equations for the hor-  
174 izontal velocity components, a mass continuity or layer thickness tendency equation, and two  
175 conservation equations for a pair of thermodynamic variables, such as salt and temperature or  
176 salt and density. The authors also define several diagnostic equations to control the spacing and  
177 movement of layer interfaces. This includes the hydrostatic equation which links temperature,  
178 salinity, and pressure, alongside an equation prescribing the vertical mass flux through a surface.  
179 A hybrid grid-generating technique determines whether isopycnal or inflated non-isopycnal layers

180 are specified [1]. Beyond the general governing equations and gridding algorithm, HYCOM has  
 181 specialized mixing processes, many of which are shared with the MICOM implementation.  
 182 Temperature and salinity profiles are assimilated into the ocean flow model to improve initial  
 183 analysis. The specific HYCOM implementation we use for data is the 41-layer HYCOM +  
 184 NCODA Global 1/12° Reanalysis experiment.

185 ERA5 is the fifth ECMWF reanalysis for global climate and weather features. The atmospheric  
 186 global reanalysis (HRES) includes the period from January 1950 to the present year. ERA5  
 187 reanalysis is produced using the 4D-Var data assimilation technique and model forecasts with  
 188 137 hybrid vertical sigma/pressure levels [2]. The data assimilation of ERA5 also contains an  
 189 ensemble system (EDA) of ten members for providing background error estimates. The model  
 190 assimilates as many observations as possible in the upper air and near-surface regions. This  
 191 forecasting system includes over a decade of research and development for all components: at-  
 192 mosphere, land, and ocean waves. The integrated forecast system (IFS) implemented by ECMWF  
 193 has its equations expertly discussed in the documentation manual [37] and is more generally  
 194 discussed in [2]. We specifically use the ERA5 hourly data on single levels from 1959 to the  
 195 present [38], which is a data assimilative reanalysis that uses the 2016 version of the ECMWF  
 196 numerical weather prediction model and data assimilation system (IFS Cy41r2). The ERA5  
 197 implementation is modeled at 1/4° latitude/longitude increments. Thus, the resolution of ERA5  
 198 is lower than that of HYCOM.

199 Given these arbitrarily complex numerical models, which are pre-computed, we do not need  
 200 to implement the PDEs which govern the models directly. Instead, we will use the outputs from  
 201 both models as training and regularization data within our deep learning models. To yield discrete  
 202 value forecasting in a generic manner, we only need the values which are geographically closest  
 203 to the latitude and longitude of the buoy observations. Likewise, we collect the discrete time  
 204 step temporally closest to the observations we are interested in. Therefore, we consider a generic  
 205 method for retrieving data from full-coverage numerical models in (1).

$$f_m(t, x, y) = v \quad (1)$$

206 For a sufficiently complex model  $f_m$ , we input the desired period  $t$  and the closest possible  
 207 latitude and longitude,  $x$  and  $y$ . This yields whichever set of scalar features  $v$  are desired from the  
 208 numerical model. These values can then be used as regularization data, training data, or both for  
 209 a deep learning PINN model. This formulation is useful in our methodology where we want to  
 210 train a neural network on the observations themselves while regularizing with numerical model

211 data. This differs to similar PINNs that provide full-coverage modeling of ocean and climate  
212 features, where the training data is limited to full-coverage reanalysis and the regularizing PDEs  
213 are formulated from simpler equations as seen in [32] [33] [34].

### 214 *B. Data and Feature Processing*

215 Both buoy observations and numerical model outputs are publicly available and have decades  
216 worth of data. In this study, we select dates from January 1st, 2011, to December 31st, 2011. The  
217 buoy data, which comprises the observation data for this study, comes from three-meter discus  
218 Self-Contained Ocean Observations Payload (SCOOP) sensor package buoys and Waverider  
219 buoys. We select 124 candidate buoys from around the United States East and West Coasts,  
220 the Caribbean, and the Gulf of Mexico. The buoy data is collected from the National Oceanic  
221 and Atmospheric Administration (NOAA) public data center. NOAA arranges individual buoys  
222 systematically by assigning each one a distinct ID number. The specific ID corresponding to each  
223 buoy selected for analysis is found in the Appendix. Water temperature, air pressure, and gust  
224 strength are extracted from the buoy feature set to provide the real-world recorded result. Since  
225 HYCOM and ERA5 are both gridded datasets, we select the data points which match the latitude  
226 and longitude as closely as possible to each buoy position. HYCOM snapshots are taken every  
227 three hours, and most buoys are recorded at the 50th minute of each hour. Therefore, we forecast  
228 buoy features in three-hour increments. To facilitate the coupling of the numerical models and  
229 buoy data, we select buoy features that have matching modeled numerical features. Out of the  
230 eighteen selected features, water temperature, gust strength, and air pressure are shared by the  
231 numerical models and the buoys, so they will be coupled in training time, as described by the  
232 loss function. We display all features recorded from the buoys and numerical models in Table I  
233 along with their original units.

234 It is possible that data is missing from our data sources in two separate ways. A value may  
235 be missing temporally such that no data is recorded at all for a particular time step. This is  
236 most common in the NOAA buoy data where, for example, a buoy faces mechanical failure and  
237 cannot record observations for days to months at a time. Therefore, our training and testing data  
238 is limited by the amount of available buoy-recorded data. The numerical models do not leave  
239 a time step without data except in one case, a 24 hour gap found within the HYCOM dataset.  
240 Since this represents only eight data points, we cover the temporal gap by replacing the missing  
241 time steps with the previous 24 hour period. Otherwise, for a given time step, features may be

TABLE I  
DATA FEATURES AND THEIR SOURCES. IN BOLD ARE NUMERICAL MODEL FEATURES TO BE COUPLED AS A  
REGULARIZATION MECHANISM WHEN FORECASTING BUOY OBSERVATIONS.

Feature Name	Feature Units	Feature Source
Water Temperature	°C	Buoy
Gust Strength	m/s	Buoy
Air Pressure	hPa	Buoy
<b>Water Temperature</b>	°C	<b>HYCOM</b>
Salinity	psu	HYCOM
Surf Elevation	m	HYCOM
Water Eastern Flow (U)	m/s	HYCOM
Water Northern Flow (V)	m/s	HYCOM
Wind Eastern Flow (U)	m/s	ERA5
Wind Northern Flow (V)	m/s	ERA5
Evaporation	m of w.e.	ERA5
<b>Gust Strength</b>	m/s	<b>ERA5</b>
Mean evaporation Rate	kg/(m <sup>-2</sup> s <sup>-1</sup> )	ERA5
Mean Runoff Rate	kg/(m <sup>-2</sup> s <sup>-1</sup> )	ERA5
Sea-Ice Cover (%)	[0-1]	ERA5
<b>Air Pressure</b>	hPa	<b>ERA5</b>
Cloud Cover	[0-1]	ERA5
Precipitation	m	ERA5

242 missing data and are replaced with fill values of 99, 999, 9999, or -32767, depending on the  
 243 data source and feature. Each of our sources of data exhibits at least some fill data, depending  
 244 on the geographical region or time of year. We remove all fill values from the data and, in  
 245 their place, linearly interpolate the missing values forwards and backwards for that individual  
 246 buoy or numerical model. If any numerical model data source is composed of more than 20% fill  
 247 values, we disregard that corresponding buoy from the training and testing pipeline. No buoys are  
 248 discarded for having too many fill values for the purpose of preserving as much data for training  
 249 and testing as possible. It is important to note that the retention of buoys with interpolated values  
 250 can have an impact on model accuracy.

251 The processed data is split into three datasets for training, validation, and testing. As each  
 252 buoy is missing various days, we select the train, test, and validation splits by date. Therefore,  
 253 all members of the training data are chosen from January 1st to September 13th. The validation

254 data is from September 13th to October 20th. The testing data includes the remainder of the  
255 year. Since the buoys are missing data at separate times of the year, a buoy may occasionally  
256 contribute to one dataset but not another. We specify the buoy selection in Table VI where we  
257 display the number of buoys allowed into each dataset. There are 148,365 training instances,  
258 23,118 validation instances, and 48,039 testing instances. Among the original 124 buoys selected  
259 for processing, only 86 buoys had training, validation, and testing data available. Each feature  
260 is independently normalized between  $-1$  to  $1$  before training, using the training data minimum  
261 and maximum values. This approach is essential in deep learning to prevent data with varying  
262 scales from dominating the network's performance. As our network is trained on scaled data,  
263 we transform the network's output to its original scale for meaningful result comparison.

264 To understand the impact of first-order differenced data on our regularizing technique, we  
265 studied two separate setups. In the first, we train the models using the original values recorded  
266 by the data sources. Subsequently, we take the first-order difference to train the model on the  
267 differences between time steps. Training with differenced values to make the data stationary  
268 is seen for non-regularized RNNs [39] and physics regularized RNNs [40] when forecasting  
269 time series. Stationarity means that a time series has been stabilized such that it has consistent  
270 statistical properties, like mean and variance [41]. Non-stationary data contains trends and  
271 seasonality that may introduce bias to the surrogate models. Taking the first-order difference  
272 of our data removes trends in the training data and makes the analysis problem more forgiving.  
273 The result is that modeling using the differenced data will result in higher accuracy and a more  
274 stable forecast. The more consistent statistics also imply more accurate scaling when normalizing  
275 the test data. Non-stationary data is still useful for models with longer context windows or  
276 the addition of features which are embedded in time, so testing both data representations is  
277 worthwhile. In our experiments, we will clearly denote the data used when training or evaluating  
278 a surrogate model as either original data or differenced data. When comparing models which  
279 forecast the differences in data rather than the original data, we need to transform the resulting  
280 forecast back to the original scale. This transformation is computed by summing the forecast  
281  $f_t$  with the initial conditions  $x_{t-1}$ , then that value is summed iteratively with each following  
282 difference forecast in the horizon window.

### 283 *C. Deep Learning Models*

284 A PINN is made up of any general network architecture. Since we are forecasting time  
285 series, we experiment on architectures that utilize GRU units, LSTM units, and Transformer  
286 units. Layers of these units are accompanied by dense fully connected layers, normalization  
287 layers, and training dropout layers. Each layer includes a non-linear activation function except  
288 for some dense layers, which are linear in the Transformer architecture. Between the layers,  
289 we add dropout layers with 5% dropout rate during training for the Transformer and 10% for  
290 the LSTM. Similarly, we apply a normalization layer in between dense and LSTM layers to  
291 prevent exploding or vanishing gradients. The Transformer block is made of ten attention heads.  
292 The exact summary of the LSTM-based and Transformer-based models can be seen in Tables  
293 II and III. The GRU-based model architecture is the same as the LSTM model. The number of  
294 trainable parameters is lesser for the GRU compared to the LSTM but is otherwise the same  
295 structure. The GRU and LSTM models have much fewer weights than the Transformer based  
296 model, which takes longer to train. We include each layer of the model, the number of trainable  
297 parameters, and the activation at that layer, if any. The GRU and LSTM models are trained for  
298 100 epochs while the Transformer model is trained for 200 epochs, due to the increased number  
299 of trainable weights. A data batch size of 256 was used in all cases. To optimize the value in  
300 each epoch of back-propagation, the Adam optimizer is selected for the Transformer model and  
301 RMSProp for the LSTM and GRU networks. The models are always trained using the same  
302 random seed to ensure experiments are as uniform as possible.

303 Each model, once initialized, is trained to accept the 18 specified features as input and produce  
304 the predicted next step for each feature as output. Since each model is trained to produce the  
305 same outputs it requires as inputs, this is considered a rolling forecast model. In this approach,  
306 to forecast further into the future, we may use the model's own outputs from time  $t$  as inputs for  
307 forecasting time  $t + 1$ . This forecasting technique depends on accurate initial values. Only the  
308 first forecast in a period,  $t_0$ , is provided with initial conditions, and as time progresses, inherent  
309 chaos or model error will compound within forecasts. This method yields models which are  
310 not constrained to a single forecast horizon. Instead, the models are more flexible, and can  
311 generically forecast any number of desired periods, once provided initial values. Using the  
312 numerical model data as inputs to our deep learning models may be considered self-fulfilling  
313 because reanalysis data includes high-quality features assimilated with ground truths not yet

TABLE II  
LSTM MODEL ARCHITECTURE. THERE ARE 24 TOTAL LAYERS WITH 2,348,546 TRAINABLE PARAMETERS. N REPRESENTS  
A VARIABLE BATCH SIZE.

Layer Type	Output Shape	Param #	Activation
Input Layer	(N, 18, 1)	0	None
Reshape	(N, 1, 18)	0	None
Dense	(N, 1, 256)	4864	Tanh
Batch Normalization	(N, 1, 256)	1024	None
Dropout	(N, 1, 256)	0	None
LSTM	(N, 1, 256)	525312	Tanh
Dropout	(N, 1, 256)	0	None
LSTM	(N, 1, 256)	525312	Tanh
Dense	(N, 1, 256)	65792	Tanh
Batch Normalization	(N, 1, 256)	1024	None
Dropout	(N, 1, 256)	0	None
LSTM	(N, 1, 256)	525312	Tanh
Dropout	(N, 1, 256)	0	None
LSTM	(N, 256)	525312	Tanh
Dropout	(N, 256)	0	None
Dense	(N, 200)	51400	Tanh
Dropout	(N, 200)	0	None
Dense	(N, 200)	40200	Tanh
Dropout	(N, 200)	0	None
Dense	(N, 200)	40200	Tanh
Dropout	(N, 200)	0	None
Dense	(N, 200)	40200	Tanh
Dropout	(N, 200)	0	None
Dense	(N, 18)	3618	Tanh

314 observed. We point out that the assimilated data and observations are only used in training time  
315 and when seeding initial values into the model. The subsequent predictions use the results from  
316 the previous prediction cycle. All else is kept equal among the models, so we may measure the  
317 effects of our methodology across multiple experiments.

318 To train the models, the loss function for our PINN is designed such that the outputs from  
319 numerical models are coupled with buoy-extracted real-world values. To do this, a weighted ratio  
320 term is used to determine how much of the calculated error comes from the residual of buoy  
321 observations versus the residual of the HYCOM and ERA5 modeled features. This combination

TABLE III  
 TRANSFORMER MODEL ARCHITECTURE. THERE ARE 21 TOTAL LAYERS WITH 13,619,190 TOTAL TRAINABLE  
 PARAMETERS. N REPRESENTS A VARIABLE BATCH SIZE.

Layer Type	Output Shape	Param #	Activation
Input Layer	(N, 18, 1)	0	None
Reshape	(N, 1, 18)	0	None
Dense	(N, 1, 512)	9728	Linear
Batch Normalization	(N, 1, 512)	2048	None
Transformer Block	(N, 1, 512)	11016692	Selu
Dropout	(N, 1, 512)	0	None
LSTM	(N, 1, 512)	2099200	Tanh
Dropout	(N, 1, 512)	0	None
Dense	(N, 1, 512)	262656	Linear
Dropout	(N, 1, 512)	0	None
Batch Normalization	(N, 1, 512)	992	None
Dense	(N, 1, 200)	2048	Linear
Dropout	(N, 1, 200)	0	None
Dense	(N, 1, 200)	102600	Linear
Dropout	(N, 1, 200)	0	None
Dense	(N, 1, 200)	40200	Linear
Dropout	(N, 1, 200)	0	None
Dense	(N, 1, 200)	40200	Linear
Dropout	(N, 1, 200)	0	None
Flatten Layer	(N, 200)	0	None
Dense	(N, 18)	3618	Linear

322 is completed for all coupled buoy features, i.e., water temperature, gust strength, and surface air  
 323 pressure. Thus, the piece-wise cost can be calculated as follows in Equations (2)-(7).

$$\Delta_1 = |\hat{y}_{\text{obs}} - y_{\text{obs}}| \quad (2)$$

$$\Delta_2 = |\hat{y}_{\text{obs}} - f_m(t, x, y)| \quad (3)$$

$$\Omega_{\text{coupled feature loss}} = \lambda * \Delta_1 + (1 - \lambda) * \Delta_2 \quad (4)$$

326 The two  $\Delta$  terms defined in (2) and (3) represent the absolute error between the predicted  
 327 observation and the observation ground truth followed by the absolute error of the predicted  
 328 observation and the numerical model output as defined in (1). The two error terms are weighted

329 by  $\lambda$ , as seen in (4). The selected  $\lambda$  value represents a ratio to determine how much weight is  
 330 provided to each ground truth. This coupled feature loss is only calculated for those features  
 331 which have both an observational and modeled collection of data available. Through additional  
 332 feature collection, the technique can be extended to couple any number of observation features  
 333 to numeric models.

$$334 \quad \Omega_{\text{modeled feature loss}} = |\hat{y}_{\text{model}} - f_m(t, x, y)| \quad (5)$$

$$\Omega_{\text{observed feature loss}} = |\hat{y}_{\text{obs}} - y_{\text{obs}}| \quad (6)$$

335 The remaining uncoupled features, as seen in (5) and (6), are used to collect loss in a more  
 336 traditional way. Excluding the coupled features from the calculation, numerical feature forecasts  
 337 are measured against numerical model values only and forecasted observational data are measured  
 338 against observational ground truth only. We include additional numerical features in our setup,  
 339 which were identified in Table I. There do not exist any non-coupled observational features, so  
 340  $\Omega_{\text{observation forecast loss}} = 0$ , in this experiment. There is no  $\lambda$  controlling the coupling ratio in the  
 341 case of (5) and (6). The final loss function which combines the disparate loss calculations can  
 342 be summarized in (7).

$$\Omega_{\text{total loss}} = \Omega_{\text{coupled forecast loss}} + \Omega_{\text{numeric forecast loss}} + \Omega_{\text{observation forecast loss}} \quad (7)$$

343 The addition of a coupled loss component is rationalized by considering that as the  $\lambda$  value  
 344 approach 0.0, we are training our model to behave more like the numerical model,  $f_m(t, x, y)$ .  
 345 Conversely, as the  $\lambda$  values approach 1.0, we are promoting forecasts which more closely  
 346 resemble the observations,  $y_{\text{obs}}$ . Expanding the example, when  $\lambda = 0.5$ , the model balances  
 347 agreement between both sources equally. In our experiments, the ground truth is measured using  
 348  $y_{\text{obs}}$ , so when  $\lambda = 1.0$ , we are essentially training a model while using no regularization strategy.

#### 349 *D. Metrics and Testing Strategy*

350 For the original data and differenced data setups the SST, gust strength, and air pressure  
 351 are forecasted over the reserved testing data for final evaluations of each model. Test horizon  
 352 windows are conducted from one period to eight periods, where an individual period measures  
 353 data collected every three hours. Therefore, this manifests as a one-step three hour forecast  
 354 through an eight-step 24 hour forecast since each forecast step is three hours apart. Using

355 the rolling forecast property mentioned, we record the mean absolute error (MAE) and root  
 356 mean square error (RMSE) for each forecast period. The MAE is calculated as follows for an  
 357 individual buoy  $\frac{1}{N} \sum_{i=1}^N (|Y_i^p - Y_i^t|)$ , where  $N$  is the total number of time steps forecasted,  $Y^p$   
 358 is the collection of predicted ocean features, and  $Y^t$  is the collection of ground truth ocean  
 359 observations. Similarly, the RMSE is computed as  $\sqrt{\frac{1}{N} \sum_{i=1}^N ((Y_i^p - Y_i^t)^2)}$ . In analysis, the total  
 360 MAE and RMSE from our test results are collected from each buoy and then averaged to find  
 361 the global mean metrics. The best possible model will provide low value metrics for all forecast  
 362 periods and features. To verify whether the coupled loss component works as a regularization  
 363 mechanism, we evaluate for  $\lambda$  values between 0.0 and 1.0 with 0.1 step intervals. Next, we  
 364 evaluate around the best scoring  $\lambda$  values using 0.02 step intervals. The results gathered in this  
 365 way may be contrasted with the numerical model outputs from HYCOM and ERA5, which are  
 366 scored using the same metrics. Using this grid search technique, we are not guaranteed to find  
 367 the  $\lambda$  value which yields global minimal error, so we aim to highlight two behaviors instead. The  
 368 first is that there exists a value of  $\lambda$ , where the RMSE, MAE, or both are lesser than  $\lambda = 1.0$   
 369 (no regularization), for at least one feature per model. The second is that the selection of best  
 370  $\lambda$  is influenced by inconsistencies in the observation data, misalignment in the numerical model  
 371 data, and the PINN architecture.

#### 372 IV. RESULTS

373 We consider which experiments yield the lowest error metrics given various PINN model  
 374 setups, our three physical features of interest, and whether the data has been differenced or not.  
 375 Beyond providing an accurate forecast, we are primarily interested in the regularization ability of  
 376 the PINN's specialized loss function. As such, we begin by considering which values of  $\lambda$  yield  
 377 the lowest error metrics. Then, the general forecasting ability of our highest performing models  
 378 will be considered for further context. Finally, we will examine the buoy accuracy given its  
 379 geographical region to consider where our method may struggle to provide high-quality outputs.  
 380 In the Appendix, we supply Tables VII-XII to display the RMSE results gathered from our PINN  
 381 models trained on various  $\lambda$  values. In the Tables, each feature from horizons starting with three  
 382 hours (one period) and up to 24 hours (eight periods) are given to see the evolution of error  
 383 over time.

### 384 A. Selection of Best $\lambda$ Values

385 We present the best value for  $\lambda$  given variations in our PINN models and the selected coupled  
386 feature. A series of Figures display each  $\lambda$  value and corresponding error metrics per model and  
387 feature. We consider the original data best  $\lambda$  results for the GRU model in Figure 1, the LSTM  
388 model in Figure 2, and the Transformer model in Figure 3. The  $\lambda$ -based ratio regularization  
389 successfully managed to reduce the MAE and RMSE of 24 hour forecasts when compared to  
390  $\lambda = 1.0$  (no regularization). For the GRU and LSTM figures, each evaluated feature displays at  
391 least one value for  $\lambda$  which yielded more performant metrics. Using the Transformer model, the  
392 PINN-style regularization yields explicitly worse forecasts for SST and Gust, but air pressure  
393 has a reduced error when  $\lambda = 0.9$ . In this sense, each model has displayed the property of MAE  
394 and RMSE reduction for at least one feature, using the regularization technique. The reason  
395 that the Transformer model performs well in the  $\lambda = 1.0$  case is because the architecture is  
396 sufficiently complex enough to generalize the observations when trained using large amounts  
397 of data. However, the results of the air pressure forecasts imply some features benefit from the  
398 coupled loss function regardless of model complexity. The LSTM and GRU models are less  
399 complex and achieve worse test results overall, so the regularization has a larger effect on error  
400 reduction. For this reason, there exists a best performing model when  $\lambda < 1.0$  in all features.

401 We highlight that the best  $\lambda$  values are unique for each experiment. This is true when  
402 comparing the separate features in the same model and when comparing the same feature from  
403 each model. For example, the best  $\lambda$  values found in the GRU features are 0.9, 0.84, and 0.96,  
404 for SST, gust strength, and air pressure, respectively. When comparing by model, the best  $\lambda$   
405 for SST is largely separated at 0.9, 0.68, and 1.0 for GRU, LSTM, and Transformer models,  
406 respectively. The uniqueness of each  $\lambda$  selection is problematic in situations where the best  $\lambda$   
407 value significantly differs between features. Each feature is coupled using the same  $\lambda$  value,  
408 although an optimal choice for one feature may not be optimal for all features. A multiple  $\lambda$   
409 setup could allow more flexibility towards this problem.

410 In observing the change between  $\lambda$  values and their error metrics, we see some trends in each  
411 feature. The SST feature in GRU and LSTM models is inconsistent with many local minima  
412 observed. The gust strength feature displays error that is mostly consistent regardless of the  
413 selection of  $\lambda$ . However, there is a noticeable decrease in error as  $\lambda$  approaches the discovered  
414 minimal value. The most obvious trend that occurs in all PINN models is the sharp decrease

415 in error of the air pressure feature as  $\lambda$  increases. This is the sole case where a regularized  
 416 Transformer model outperforms the  $\lambda = 1.0$  case. This is likely caused by misalignment in the  
 417 ERA5 model when compared to the ground truth. Extremely divergent outliers in ERA5 mean  
 418 that training the surrogate model using numerical model data is a poor choice compared to the  
 419 observations. So, error decreases when  $\lambda > 0.5$  and the PINN produces forecasts more aligned  
 420 with the observations. Still, the ERA5 data is well-fitted outside of outlier conditions, so  $\lambda < 1.0$   
 421 promotes a regularizing effect on the model. This is an example of how our methodology can  
 422 combine multiple data sources to improve results when each has their own biases.

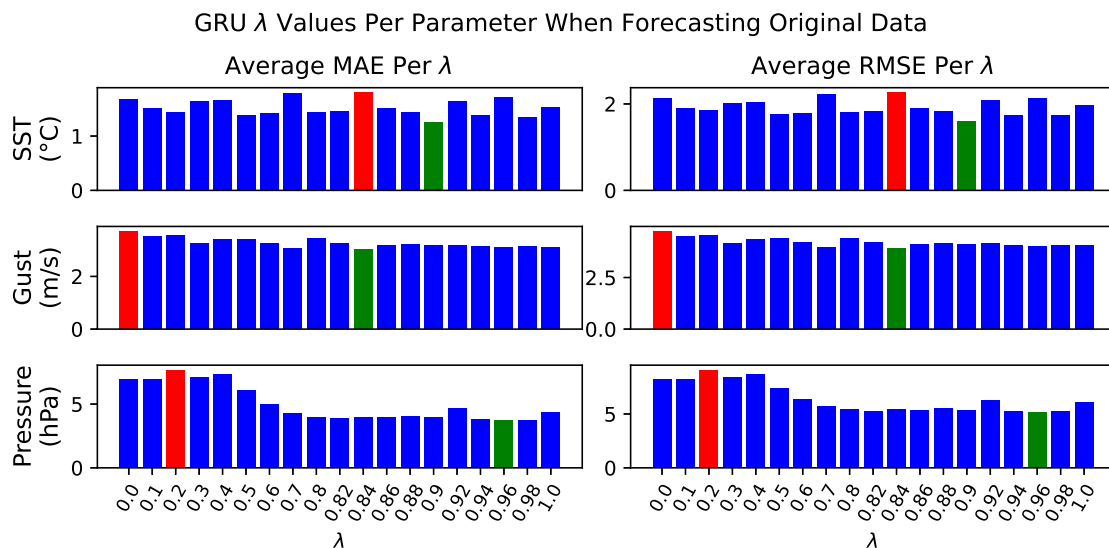


Fig. 1. MAE and RMSE for GRU forecasts from  $\lambda = 0.0$  to  $\lambda = 1.0$  (no regularization). The lowest scoring  $\lambda$  value is displayed in green while the highest is red. Forecasts are given as the original values.

423 Comparing the experimental results of the original data scheme to the results of the differenced  
 424 data scheme shows varying results. We present the differenced data best  $\lambda$  results for the GRU  
 425 model in Figure 4, the LSTM model in Figure 5, and the Transformer model in Figure 6. The  
 426  $\lambda$ -based ratio regularization scheme reduces MAE and RMSE in all but one case. As before, the  
 427 Transformer yields strictly better results when  $\lambda = 1.0$  for SST. However, the ERA5 features  
 428 show strictly best results when  $\lambda = 0.0$ , achieving lowest scores when the model is only trained  
 429 on numerical data. Considering the GRU and LSTM figures, each feature displays a minimizing  $\lambda$   
 430 that yields lower error metrics than the  $\lambda = 1.0$  case. The best  $\lambda$  values found overall are typically  
 431 closer to  $\lambda = 0.0$ . This is the exact opposite behavior when compared to the original results, and  
 432 the trend is most obvious when considering the air pressure feature. Lower values of  $\lambda$  yield

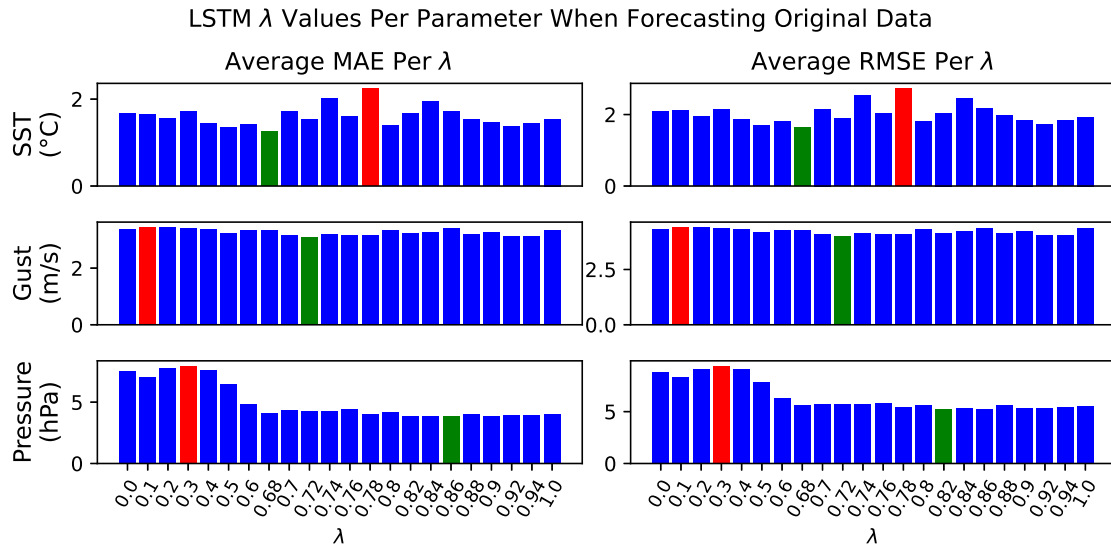


Fig. 2. MAE and RMSE for LSTM forecasts from  $\lambda = 0.0$  to  $\lambda = 1.0$  (no regularization). The lowest scoring  $\lambda$  value is displayed in green while the highest is red. Forecasts are given as the original values.

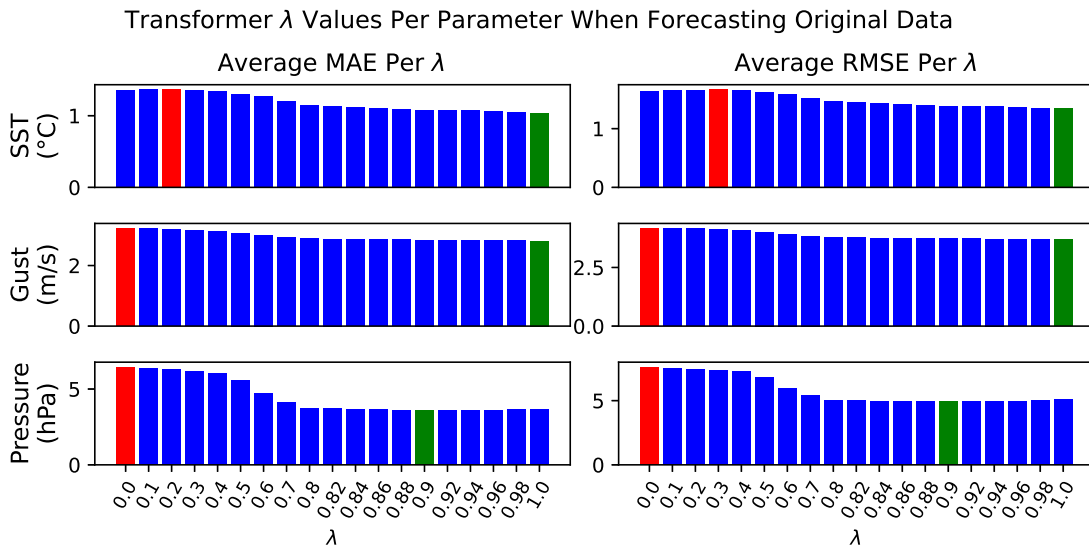


Fig. 3. MAE and RMSE for Transformer forecasts from  $\lambda = 0.0$  to  $\lambda = 1.0$  (no regularization). The lowest scoring  $\lambda$  value is displayed in green while the highest is red. Forecasts are given as the original values.

433 more performant results, although the absolute difference in error is small. Most importantly,  
 434 each model has shown error reduction for at least two features using the regularization technique.

435 The  $\lambda$  values for SST are chaotic, like before, and the best value varies greatly per model.  
 436 Conversely, the error metrics are much lower overall due to the differenced data representation.

437 The behavior of  $\lambda$  regarding the gust strength feature is similar to the original data figures for the

GRU and LSTM models. In all, the selection of a wider variety of lower  $\lambda$  values suggests that the rate of change in both datasets are alike. The numerical models also have less interpolated data which promotes more stable training. Once again, we find that most results display best  $\lambda$  values which are different between features and models. The one outlier comes from the Transformer model, where SST maintains a best result at  $\lambda = 1.0$ . Wind gust strength and air pressure both display similar values of  $\lambda$  between the GRU and LSTM models, but the SST varies drastically between each. This discussion underpins the idea that both the feature, the model, and the data representation influence the selection of best  $\lambda$ .

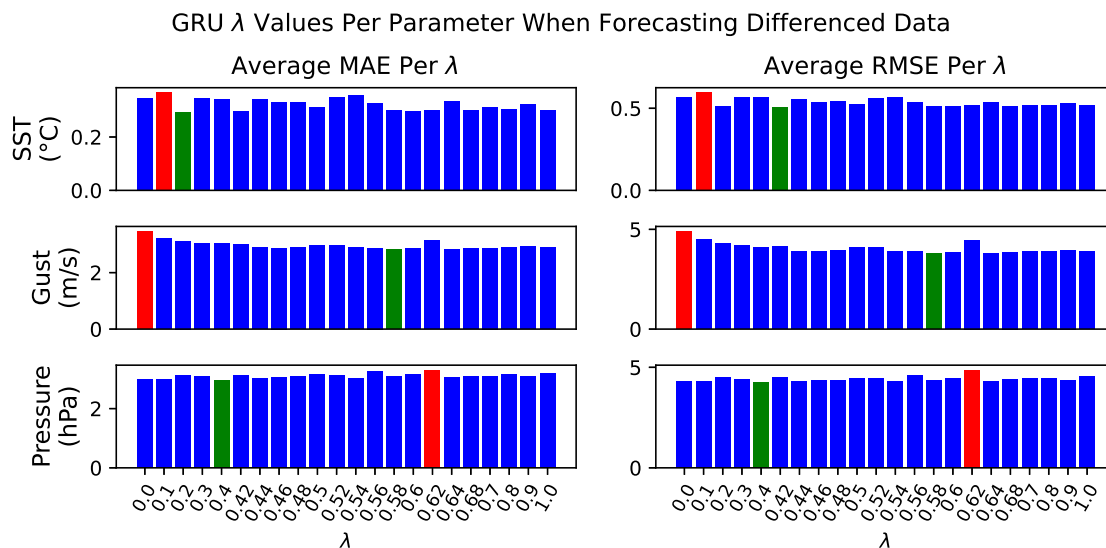


Fig. 4. MAE and RMSE for GRU forecasts from  $\lambda = 0.0$  to  $\lambda = 1.0$  (no regularization). The lowest scoring  $\lambda$  value is displayed in green while the highest is red. Forecasts are given as first-order differenced values.

In this section we considered how the selection of the best  $\lambda$  differs as the parameters of our experiments change. The Transformer model received the least benefit from  $\lambda < 1.0$  overall. For the Transformer, the SST feature never benefits from the coupled loss, air pressure is always improved, and gust speed depends on whether the data is differenced or not. Both other models benefit at least somewhat from the regularization in all cases. We learned the benefit of the regularization and the corresponding selection of best  $\lambda$  are tied to the complexity of the model, where models with fewer weights benefit more when using this methodology. Another observation is that values approaching 0.0 for  $\lambda$  tend to yield worse results unless we are considering the differenced data representation. This is due to the way each model is trained to forecast the change between time steps. When taking a first-order difference of the data, a larger

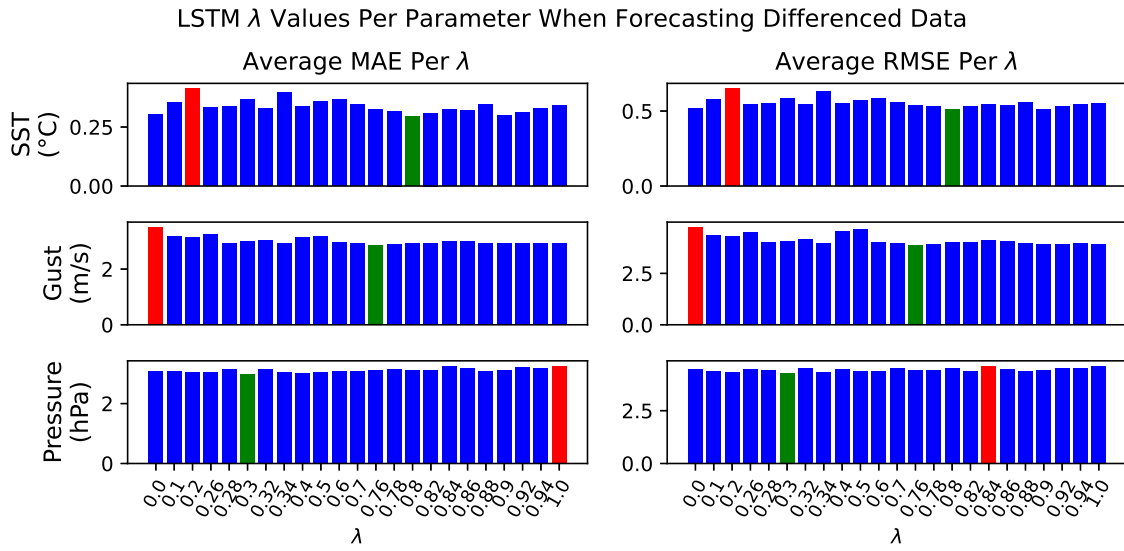


Fig. 5. MAE and RMSE for LSTM forecasts from  $\lambda = 0.0$  to  $\lambda = 1.0$  (no regularization). The lowest scoring  $\lambda$  value is displayed in green while the highest is red. Forecasts are given as first-order differenced values.

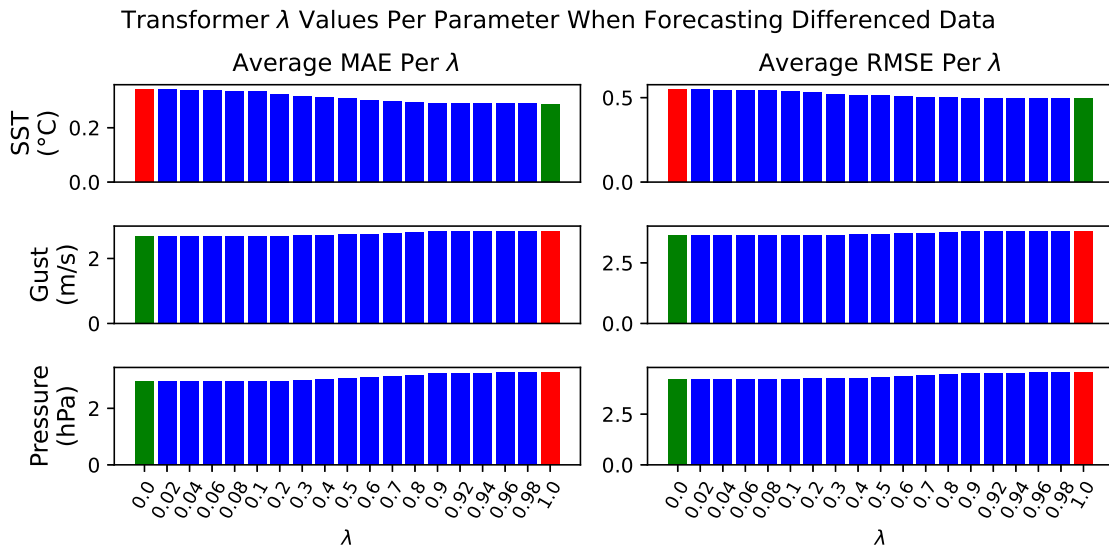


Fig. 6. MAE and RMSE for Transformer forecasts from  $\lambda = 0.0$  to  $\lambda = 1.0$  (no regularization). The lowest scoring  $\lambda$  value is displayed in green while the highest is red. Forecasts are given as first-order differenced values.

456 number of interpolated buoy observation values produces an uninformative training environment  
 457 for differenced data. The numerical models, have fewer interpolated values and more accurately  
 458 reflect change from one time to another. Therefore, PINNs which act more like the numerical  
 459 model are more performant in this case. Finally, by examining the way the best  $\lambda$  changes in  
 460 each experiment, we find that the feature, the model, and the data representation all influence

461 the selection of best  $\lambda$ . Otherwise, the best  $\lambda$  selections would be more homogeneous overall.

### 462 *B. General Forecast Accuracy*

463 By examining the general forecast accuracy of our models, we gain additional insights into  
464 the coupled loss technique used and the stability of our PINN models. To begin, we consider  
465 the measured RMSE for the best found  $\lambda$  per feature. We compare this error to those derived  
466 from the  $\lambda = 1.0$  case and from the numerical models for additional context. To facilitate this  
467 comparison, we introduce Tables IV for the original value forecasts and V for the differenced  
468 value forecasts. In these tables, we compare the percent change in RMSE between the best  $\lambda$   
469 value and  $\lambda = 1.0$  in the fourth column. In the final column, we compare the best *lambda*  
470 value to the numerical models. These values are calculated using the RMSE as found in the  
471 eight-step forecast from the Appendix Tables VII-XII. Negative values indicate a reduced error  
472 when comparing the best  $\lambda$  value to the  $\lambda = 1.0$  case or the numerical models. Positive values  
473 show when the best  $\lambda$  results are worse than the compared source of error. When the percentage  
474 is zero, the best value of  $\lambda$  for that experiment was  $\lambda = 1.0$ .

475 Examining the original value forecast results in Table IV shows that this method is rarely more  
476 performant than the numerical models. The feature SST is worse than the numerical model by  
477 at least 100%, which implies the HYCOM model is well-calibrated to local conditions. When  
478 comparing the lower resolution ERA5 model, air pressure and gust strength are less aligned with  
479 the recorded observations. As a result, the feature gust speed is up to 37% less accurate when  
480 using the PINN models and results are more accurate using all architectures for air pressure.  
481 This is encouraging and suggests that our surrogate modeling technique can produce permissible  
482 forecasts depending on the feature. The comparison of the best surrogate model to the non-  
483 regularized surrogate when  $\lambda = 1.0$  is more favorable. From the Table, we show that there  
484 is a percent decrease in error for most cases. The GRU and LSTM models are more accurate  
485 when compared to the non-regularized versions. The air pressure results show that the surrogate  
486 outperforms the numerical model only after finding the best  $\lambda$  value. That is, we only outperform  
487 the numerical model due to the coupled loss function. The Transformer models showed improved  
488 forecasts for air pressure alone. This indicates that a large network with many trainable parameters  
489 can still benefit from our technique, but the reduction in error will be less, if there is any at all.

490 Continuing, we consider the percent change in RMSE when experimenting with the differenced  
491 data representation in Table V. Overall, when comparing the PINN models to the numeric

TABLE IV  
ORIGINAL VALUE FORECAST % CHANGE IN RMSE WHEN COMPARING THE BEST FOUND  $\lambda$  AGAINST  $\lambda = 1.0$   
(NO REGULARIZATION) AND THE NUMERICAL MODEL (HYCOM/ERA5)

Model	Best $\lambda$	Feature	$\lambda = 1.00$	Numerical Model
GRU	0.90	SST ( $^{\circ}$ C)	-18.44%	+141.47%
	0.96	Pressure (hPa)	-14.83%	-3.08%
	0.84	Gust (m/s)	-3.98%	+33.11%
LSTM	0.68	SST ( $^{\circ}$ C)	-15.42%	+145.45%
	0.82	Pressure (hPa)	-4.48%	-0.78%
	0.72	Gust (m/s)	-7.62%	+37.25%
Transformer	1.00	SST ( $^{\circ}$ C)	0.0%	+102.02%
	0.90	Pressure (hPa)	-3.06%	-7.58%
	1.00	Gust (m/s)	0.0%	+26.44%

492 model, we see improvement when using this data representation. The only comparison which is  
 493 still worse than the numerical models is when forecasting the gust speed feature, although the  
 494 percentage of error is slightly decreased. Almost all the features show decrease in error when  
 495 comparing the best  $\lambda$  to the model trained when  $\lambda = 1.0$ . The spread of the decrease in error  
 496 is lesser than when forecasting the original data, with the highest at about 8% and the lowest  
 497 at 1.6%. There is no situation for this data where the best  $\lambda$  directly causes improvement over  
 498 the numerical model, but we find an increased performance gap between the deep learning and  
 499 numerical models in most cases.

500 We also consider the stability of the forecasts, given a single example buoy. In Figure 7 and  
 501 Figure 8 we show how the error of our PINNs evolves over the forecast period of 24 hours given  
 502 chaotic features, model architectures, and data representations. These figures capture a subset  
 503 of 10 forecast periods, from time step 40 to time step 120, for a single buoy. The ground truth  
 504 values are reinitialized into the model every eighth time step, hence the ten forecast periods.  
 505 To select the  $\lambda$  value to represent in the figures, we use the best  $\lambda$  value found for SST. When  
 506 SST does not have a best  $\lambda < 1.0$  then the best value for gust strength or air pressure was  
 507 chosen. This highlights the limiting factor of our technique in its current form, as it cannot  
 508 utilize multiple values for  $\lambda$ . Future explorations into this technique might consider a multiple  
 509  $\lambda$  setup for more flexibility.

TABLE V  
DIFFERENCED VALUE FORECAST % CHANGE IN RMSE WHEN COMPARING THE BEST FOUND  $\lambda$  AGAINST  
 $\lambda = 1.0$  (NO REGULARIZATION) AND THE NUMERICAL MODEL (HYCOM/ERA5)

Model	Best $\lambda$	Feature	$\lambda = 1.00$	Numerical Model
GRU	0.42	SST ( $^{\circ}$ C)	-1.64%	-23.43%
	0.40	Pressure (hPa)	-6.30%	-20.10%
	0.58	Gust (m/s)	-2.89%	<b>+29.73%</b>
LSTM	0.80	SST ( $^{\circ}$ C)	-7.45%	-23.19%
	0.30	Pressure (hPa)	-7.18%	-19.66%
	0.76	Gust (m/s)	-2.18%	<b>+31.46%</b>
Transformer	1.00	SST ( $^{\circ}$ C)	<b>0.0%</b>	-25.63%
	0.00	Pressure (hPa)	-7.93%	-20.72%
	0.00	Gust (m/s)	-4.80%	<b>+24.45%</b>

510 When examining the original data forecast results for buoy 42002 in Figure 7, it is expected  
511 for error to increase over the period. Ideally, the error of the best found  $\lambda$  will increase more  
512 slowly than when  $\lambda = 0.0$  or  $\lambda = 1.0$ , for each feature. From this figure, we can observe that  
513 error increases until the model is realigned with fresh initial values. We see that the forecasts  
514 are often worse than the numerical model. They are typically most performant around time steps  
515 one or two, when the initial values are still relatively recent. Comparing models and features  
516 shows a wide variety of behaviors. The most similar forecasts are found when considering the  
517 Transformer, when each of the PINN models performs almost identically. The GRU models tend  
518 to disagree the most between each of the specific experiments, which makes sense considering  
519 it achieves the highest reduction in forecast error overall. PINNs are traditionally used to reduce  
520 numerical instability, and this behavior can be seen when forecasting air pressure using the GRU  
521 model. Between time steps 56 and 64, the best-selected  $\lambda$  shows significantly reduced error when  
522 comparing to the  $\lambda = 1.0$  case. The same temporal region in the Transformer forecast displays  
523 the opposite behavior where the non-regularized model performs better than any regularized  
524 version. This is due to the complexity of the Transformer-based architecture which causes the  
525 model to generalize underlying behaviors more effectively than the GRU or LSTM architectures.

526 Finally, we compare the differenced value forecast MAE scores for buoy 42002 from the  
527 Figure 8. In the case of the Transformer model, we show  $\lambda = 0.5$  because each feature's best  $\lambda$

528 lies on the extreme end of either  $\lambda = 0.0$  or  $\lambda = 1.0$ . The main benefit of using the differenced  
529 data representation is displayed by the reduction in overall error across all models. The Figure  
530 demonstrates how the  $\lambda$  forces the PINN to behave more like one data source or the other,  
531 evidenced by the fact that the MAE found tends to be bound by the other error sources. Overall,  
532 error increases more slowly in regions where the forecasted feature remains highly stable over  
533 time. Once again, we see that refreshing the initial values reduces error significantly, which is  
534 the expected behavior. The error spread between the PINN is much more similar in this case  
535 because the models rely more on autocorrelation between forecast periods. Error reduction is  
536 significant enough to suggest the regularized models make more informed forecasts on average.  
537 It is significant to note that individual plots of forecasts from the best  $\lambda$  model may be less  
538 accurate than other setups in specific instances, but error is reduced overall when considering  
539 all buoys.

540 In this section, we analyzed the forecasting ability of our models by considering percent  
541 reduction in errors and the forecast of a single buoy via different experimental permutations.  
542 The selection of  $\lambda$  and total amount of error reduction was shown to depend on the model,  
543 the features examined, and the data representation used. When compared to models where  $\lambda =$   
544 1.0, percentage reductions in error were as low as 1.6% and as high as 18.4%. When using  
545 the Transformer model, the feature SST never showed improvement over the  $\lambda = 1.0$  case.  
546 The surrogate models always outperform the numerical model for the air pressure feature and  
547 outperform in SST forecasting depending on the data representation. We never outperform the  
548 numerical model when forecasting gust strength. In the case of feature air pressure, the error  
549 reduction from selecting  $\lambda$  through a grid search allows the surrogate PINN model to out-perform  
550 the numerical model. It is important to restate that the interpolated values in the ground truth  
551 provide some bias in the test by penalizing the numerical models when comparing to those  
552 interpolated values. In addition, inference based on differenced inputs produces more stable  
553 estimates of local conditions, i.e., the observations. Our surrogate models benefit from both  
554 points which explains the general improvement when compared to the numerical model. More  
555 importantly, selecting the best regularization parameter,  $\lambda$ , yields models that achieve higher  
556 accuracy, and this is consistent across both data representations. We showed how the error in  
557 forecasts are reduced on average by training the surrogate model using the selected  $\lambda$  value. This  
558 revealed the way model selection and data representation affects the numerical stability over the  
559 forecast period. The differenced data representation simplifies the problem for the surrogate

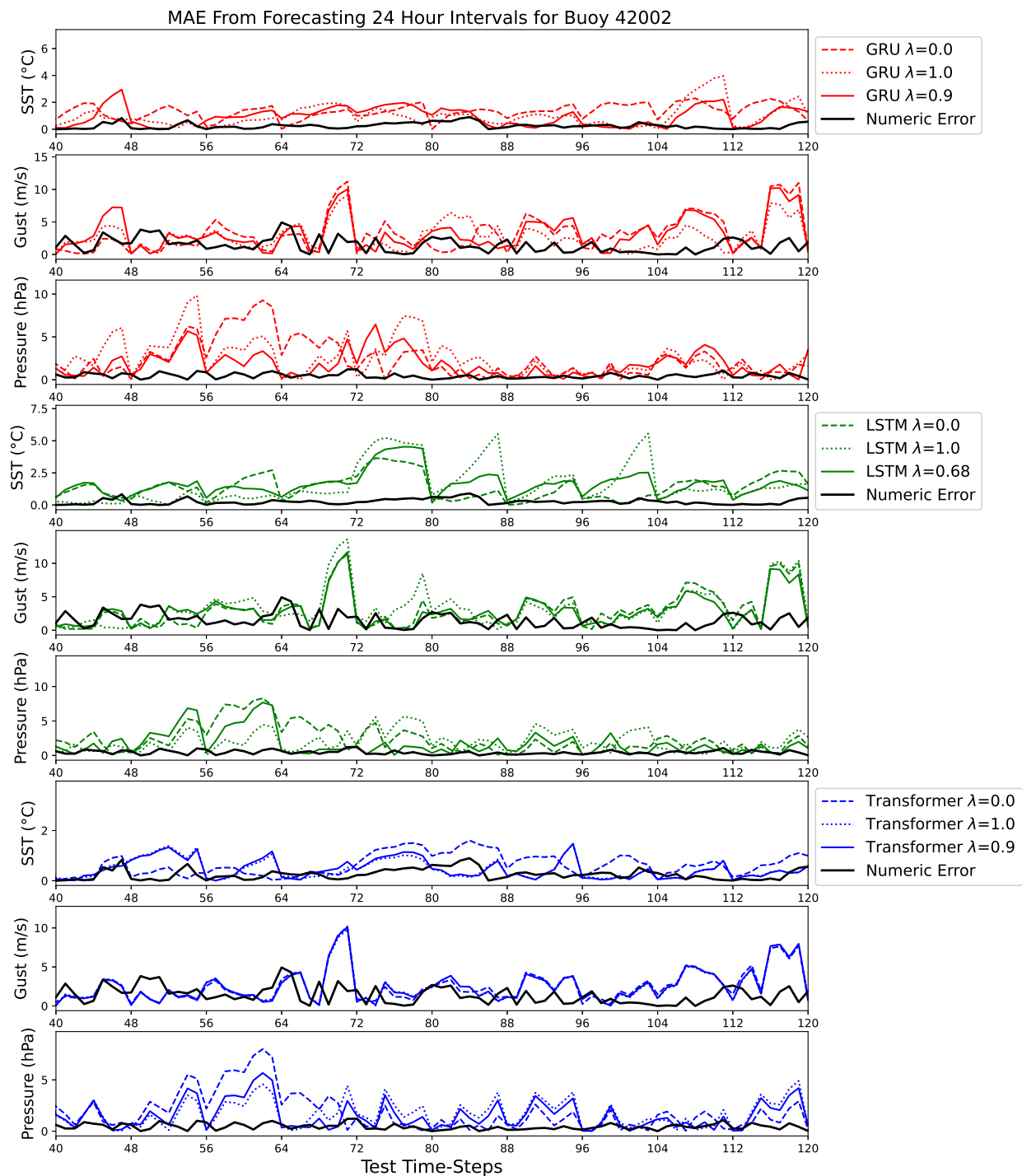


Fig. 7. The numerical and surrogate model MAE for each feature over ten 24-hour forecast periods is displayed. We include each PINN with  $\lambda = 0.0$ ,  $\lambda = 1.0$  (no regularization), and the best found  $\lambda$ . The PINNs are reinitialized with new starting values every eighth period.

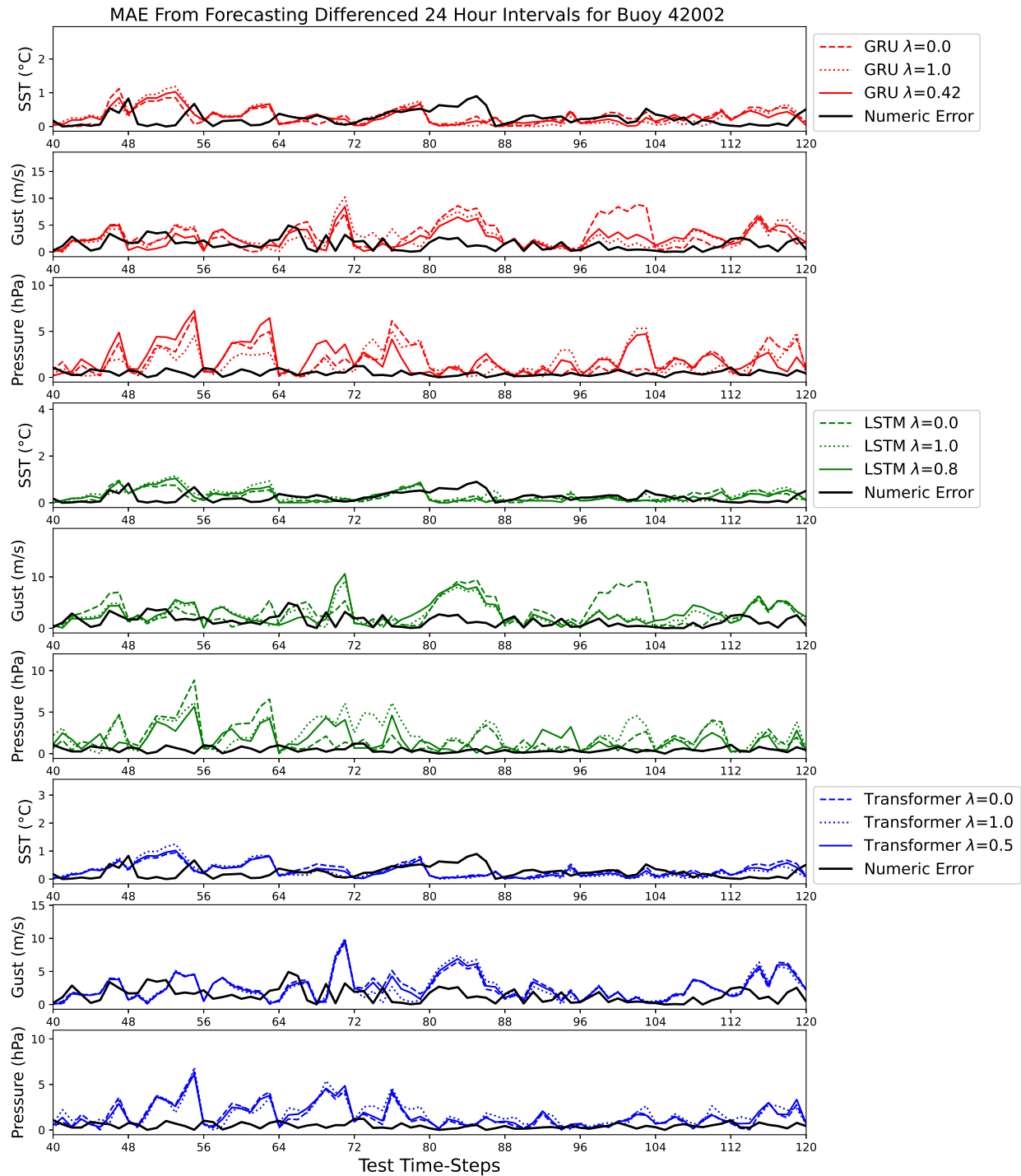


Fig. 8. The numerical and surrogate model MAE for each feature over ten 24-hour forecast periods is displayed. Differenced value forecasts have been transformed back to the original scale before finding the error. We include each PINN with  $\lambda = 0.0$ ,  $\lambda = 1.0$  (no regularization), and the best found  $\lambda$ . The PINNs are reinitialized with new starting values every eighth period.

560 models, so the forecast stability remains similar between models and features. The opposite is  
561 true in the original data forecasts, which is more chaotic and showed disagreements. In all, the  
562 analysis of these results suggest that our model is relatively stable over 24 hour periods, but  
563 error is often worse than the reanalysis models when they are well-fitted to the observation data.

### 564 *C. Geographical Error Analysis*

565 Our final method for comparing the numerical models with our PINNs involves an analysis of  
566 buoy RMSE per their geographical position. To this end, we provide two figures which represent  
567 a grid of our models as rows with the forecasted feature as columns. Positional markers reference  
568 the latitude and longitude of each buoy, and there is overlap due to the number of buoys. The  
569 color bar represents the amount of RMSE calculated for a buoy and is normalized column-wise  
570 by the minimum and maximum error generated for the feature by each model. In Figure 9 we  
571 show the results from the original data forecast and in Figure 10 we show the results from the  
572 differenced dataset. One caveat to these figures is that we cap the error of the air pressure feature  
573 in both figures to a max value of 10. This is because the ERA5 has an extreme misalignment  
574 in outlier areas, which dominates the color interpolation. We cap the error derived from SST to  
575 a max value of one in the differenced Figure 10 for the same reason.

576 The original values forecast results in Figure 9 show there are some trends among the models.  
577 First, the best performing region for all features are the forecasts of buoys clustered around the  
578 Caribbean. The Gulf of Mexico region performs similarly but can be slightly less accurate de-  
579 pending on the experiment. The least performant regions tend to be along the North Atlantic East-  
580 Coast and various regions around the Pacific West-Coast. The numerical models are, on average,  
581 are extremely well fitted to real-world observations. Although, there are cases, possibly due to  
582 resolution constraints of grid data, where massive influxes of error are found. This misalignment  
583 shows the benefit of local condition forecasting. For example, the numerically modeled outliers  
584 for air pressure are along the West-Coast. These same regions perform well using our technique  
585 because we model the forecast based on local observed conditions. Geographic regions which  
586 are poorly forecasted by a PINN model tend to cluster among similarly performing regions. We  
587 do not observe alternating high and low error regions, which would imply random forecasts.  
588 Instead, we very consistently see gradients of low to high error regions. This may be explained  
589 by considering that some regions may pose a modeling challenge due to geography, river runoff,  
590 human operations, lack of data, and so on.

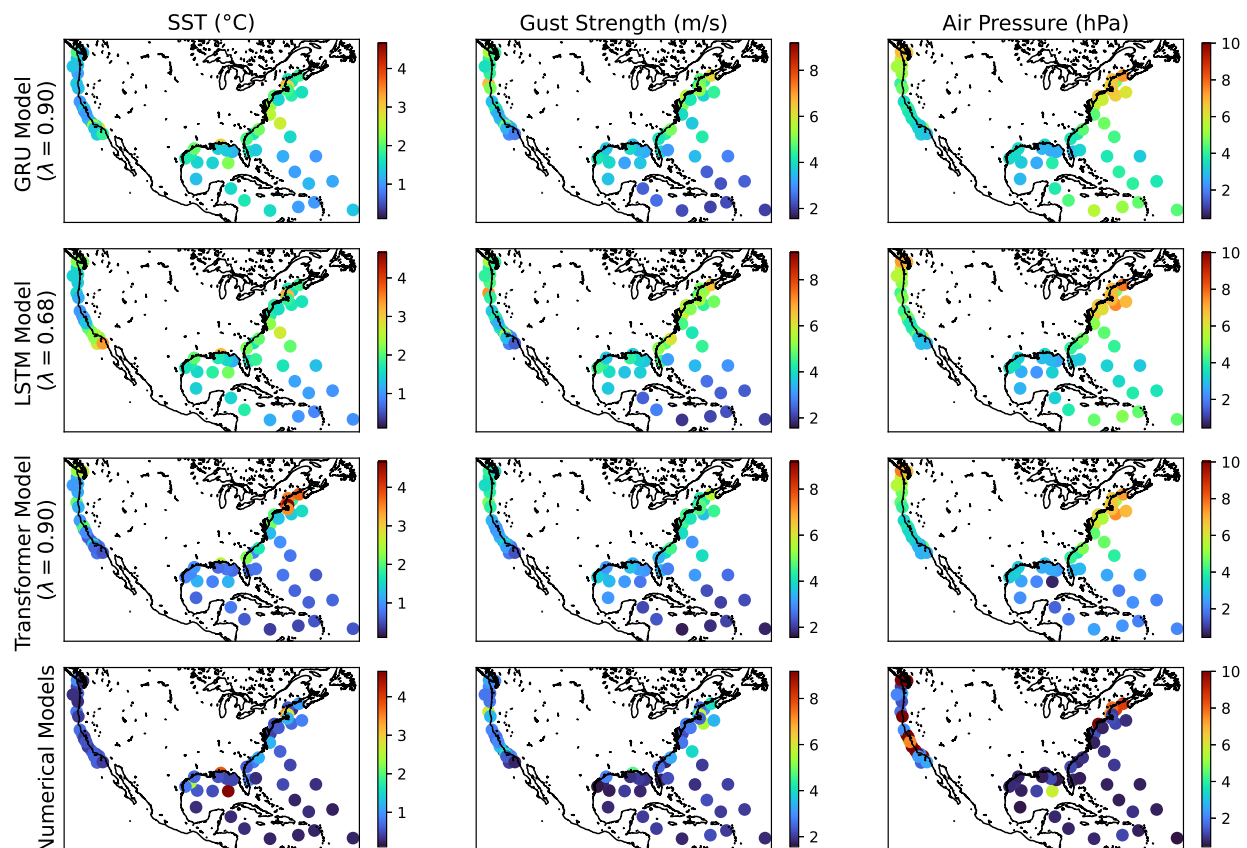


Fig. 9. Analyzed original features (columns) compared to the generating model (rows) by RMSE given at the geographical buoy location. Error is capped for SST and air pressure for visualization purposes. Color maps are normalized by each feature for comparative evaluation.

591 Next, we analyze the difference valued forecast results in Figure 10. The results are more  
 592 homogeneous and more accurate across all models and features. Compared to the original  
 593 forecast, similar geographical zones display relatively high errors, showing these are likely  
 594 regions of high change. Each of the PINN models yields similar error scores which suggests that  
 595 they rely on low-change forecasts to accurately describe the true value. Therefore, the models  
 596 produce more similar results and are more sensitive to chaotic regions. From the Figure, we can  
 597 pick out an instance of an outlier buoy in the center of the Caribbean region, when forecasting  
 598 the SST parameter. There, error from HYCOM is high while the error from each PINN model  
 599 is low. In this case, the numerical model represents real world conditions and error is calculated  
 600 through interpolated initial values, causing inflated metrics. However, this is not the reason for  
 601 all outliers. In the case of air pressure, most high-error regions are a case of misalignment in  
 602 the numerical model.

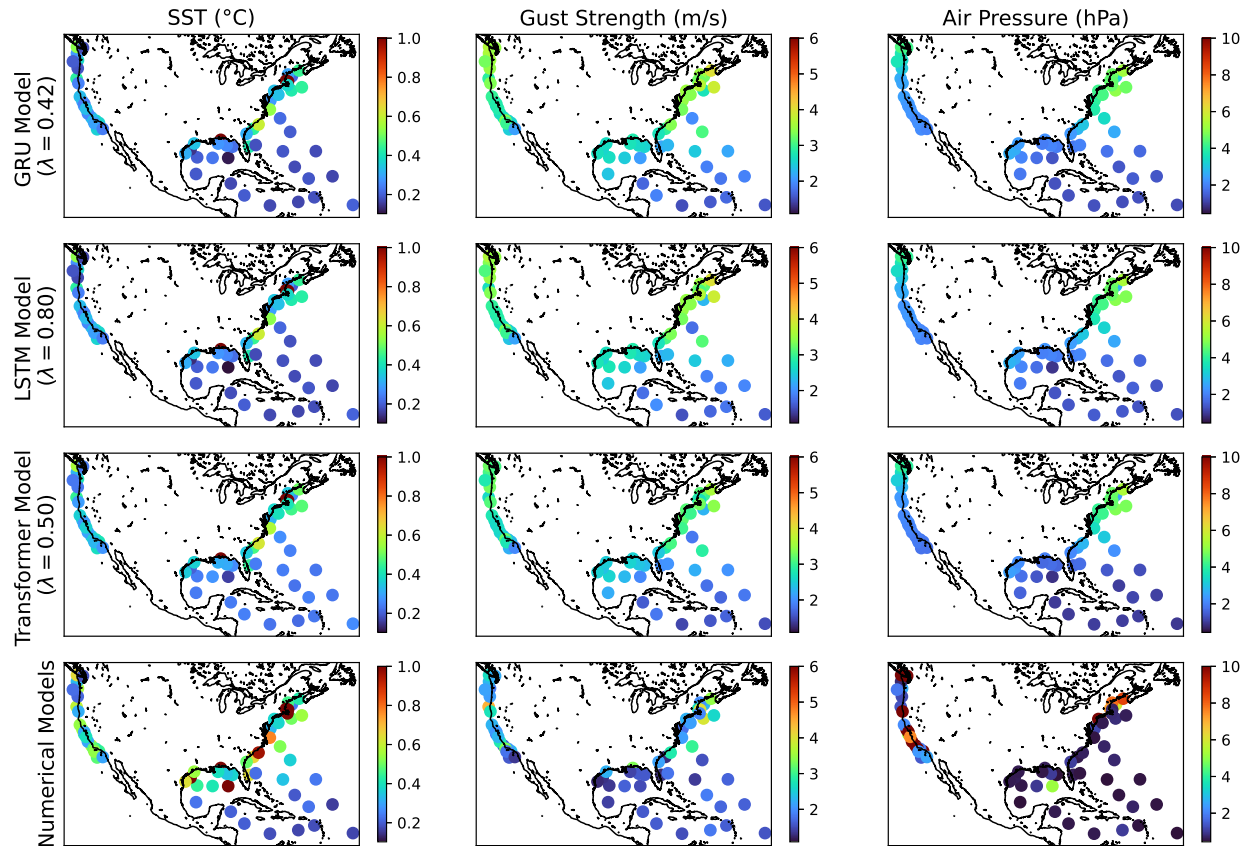


Fig. 10. Analyzed differenced features (columns) compared to the generating model (rows) by RMSE given at the geographical buoy location. Error is capped for SST and air pressure for visualization purposes. Color maps are normalized by each feature for comparative evaluation.

603 By examining the individual buoy error, we learned which geographic regions are most difficult  
 604 to model. We also revealed patterns in the similarities between our PINN experiments and the  
 605 numerical models. The figures revealed that the numerical models have some regions with high  
 606 error. The error is mainly found when there is misalignment in the numerical models. Some  
 607 error was introduced through our interpolation scheme, such as the SST outlier in the Gulf of  
 608 Mexico. Buoys which received low accuracy forecasts tend to be surrounded by buoys with  
 609 similar metrics, which implies they are within difficult-to-model geographical regions. Although  
 610 the error for the differenced data representation is lower than when forecasting the original  
 611 values, the buoys with the highest error come from similar regions. When comparing our sparse  
 612 forecasting technique to a full-coverage model, our method is not constrained to a grid region,  
 613 and any arbitrary point may be modeled. Therefore, error may be reduced when forecasting  
 614 regions between vertices, without relying on interpolation techniques. The drawback of using

615 this sparse forecasting technique is that greater spatial conditions cannot be deciphered by the  
616 observations alone. In this way, we trade off providing regional context to the PINN model for  
617 increased forecasting flexibility. The PINN architecture bases the forecast off current conditions  
618 alone and is independent of the buoy's geography.

## 619 V. CONCLUSIONS

620 We investigated the ability of the ocean flow model HYCOM and the climate model ERA5  
621 to be used as regularization data for PINN-inspired deep learning models. A special formulation  
622 of the loss function yielded comprehensive models for forecasting any number of physical  
623 parameters in a sequence-to-sequence model. The techniques demonstrated how multiple ocean  
624 and climate features may be forecasted and combined using deep LSTM, GRU, and Transformer  
625 physics-informed networks. Our sparse feature forecasting approach yielded more flexible, gener-  
626 alized models, which are less constrained to predefined regions. In contrast to other PINN models,  
627 we train the models using observation data while regularizing with pre-computed numerical  
628 models. The significance of this is that we do not need to implement the numerical formulation for  
629 use in our framework. In most cases, we improved the surrogate model performance by combining  
630 the observation data and numerical models. To assess the models, we set up experimental sparse  
631 sequential forecasting procedures for SST, air pressure, and gust strength as observed by free  
632 floating buoys. Two separate data representations were investigated which included the original  
633 observed/modeled data and first order differenced versions of the data. Over these experiments,  
634 the hyperparameter  $\lambda$  was fine-tuned between 0.0 and 1.0 to find the best possible data ratio. We  
635 found that models which have a less complex architecture improved the most from the inclusion  
636 of the numerical model regularization. This was shown explicitly by comparing the results of the  
637 least complex and most complex architectures of the GRU and Transformer models. The GRU  
638 and LSTM models showed improvements after tuning for  $\lambda$  in every case while the Transformer  
639 models showed improvement for fewer features. Further, the selection of  $\lambda$  significantly altered  
640 the behavior of the PINN models. As the  $\lambda$  value approaches 0.0, the trained model produced  
641 results more like the numerical models, while the opposite is true when  $\lambda$  approaches 1.0.  
642 Depending on the experiment, we saw improvements over the numerical model in forecast error.  
643 In favor of our method, the PINN forecasting of air pressure showed improvement over the  
644 numerical models when the best selection of  $\lambda$  was chosen. Overall, our method improved  
645 the numerical stability of the forecasts on average over the horizon period. In the case of the

646 differenced data representation, we saw the stability of each PINN model was similar. Lower  
647 valued  $\lambda$  values were most performant in this case, which suggests the numerical model data  
648 was more informative overall. This is likely due to fewer interpolated values from the numerical  
649 models when compared to the buoy observations. The differenced data forecasts are the most  
650 accurate overall, but the amount of error reduction found when using this data representation was  
651 less. Exploring the error geographically showed us that modeling high-change areas of interest is  
652 difficult for both the numerical models and our PINNs. This methodology can be used to forecast  
653 observations between the vertices of grid-based numerical models. The trade-off of the increased  
654 flexibility is the loss of context of spatial conditions beyond the immediate forecast region.  
655 Ongoing work on this methodology continues in several ways. Because the selection of  $\lambda$  changes  
656 on a feature-by-feature basis, we should investigate an approach to allow an independent selection  
657 of  $\lambda$  values on a per-feature case. Using a grid search for selecting the best  $\lambda$  value is currently  
658 inefficient. Future improvements to our technique will revolve around fine-tuning the  $\lambda$  selection  
659 approach to reduce computational overhead of the models. Moreover, since we formulate new  
660 models that combine numerical models with observations, our framework leaves room to explore  
661 integration into a data assimilation scheme. The methodology should be expanded to combine  
662 multiple numerical models with relevant PDEs to see if similar improvements can be found when  
663 forecasting full-coverage models also. Different domain problems and experimental setups will  
664 yield further insight into this procedure for combining multiple sources of data when each has  
665 inherent limitations.

#### 666 ACKNOWLEDGMENT

667 This work was partly supported by the U.S. Department of the Navy, Office of Naval Research  
668 (ONR), and Naval Research Laboratory under contracts N00173-20-2-C007 and N00173-20-2-  
669 C007, respectively. The work of Austin Schmidt was funded by a SMART (Science, Mathematics  
670 and Research for Transformation) Department of Defense (DoD) scholarship for service.

#### 671 REFERENCES

- 672 [1] R. Bleck, "An oceanic general circulation model framed in hybrid isopycnic-cartesian  
673 coordinates," *Ocean modelling*, vol. 4, no. 1, pp. 55–88, 2002.
- 674 [2] H. Hersbach, B. Bell, P. Berrisford, *et al.*, "The era5 global reanalysis," *Quarterly Journal*  
675 *of the Royal Meteorological Society*, vol. 146, no. 730, pp. 1999–2049, 2020.

- 676 [3] G. R. Halliwell, "Evaluation of vertical coordinate and vertical mixing algorithms in the  
677 hybrid-coordinate ocean model (hycom)," *Ocean Modelling*, vol. 7, no. 3-4, pp. 285–322,  
678 2004.
- 679 [4] S. Cuomo, V. S. Di Cola, F. Giampaolo, G. Rozza, M. Raissi, and F. Piccialli, "Scientific  
680 machine learning through physics-informed neural networks: Where we are and what's  
681 next," *Journal of Scientific Computing*, vol. 92, no. 3, p. 88, 2022.
- 682 [5] M. Haghbin, A. Sharafati, D. Motta, N. Al-Ansari, and M. H. M. Noghani, "Applications  
683 of soft computing models for predicting sea surface temperature: A comprehensive review  
684 and assessment," *Progress in earth and planetary science*, vol. 8, no. 1, pp. 1–19, 2021.
- 685 [6] S. Zhang, Z. Liu, X. Zhang, *et al.*, "Coupled data assimilation and parameter estimation  
686 in coupled ocean-atmosphere models: A review," *Climate Dynamics*, vol. 54, no. 11,  
687 pp. 5127–5144, 2020.
- 688 [7] N. Barton, E. J. Metzger, C. A. Reynolds, *et al.*, "The navy's earth system prediction  
689 capability: A new global coupled atmosphere-ocean-sea ice prediction system designed for  
690 daily to subseasonal forecasting," *Earth and Space science*, vol. 8, no. 4, e2020EA001199,  
691 2021.
- 692 [8] S. Razavi, B. A. Tolson, and D. H. Burn, "Review of surrogate modeling in water  
693 resources," *Water Resources Research*, vol. 48, no. 7, 2012.
- 694 [9] X. Yu, S. Shi, L. Xu, Y. Liu, Q. Miao, and M. Sun, "A novel method for sea surface  
695 temperature prediction based on deep learning," *Mathematical Problems in Engineering*,  
696 vol. 2020, 2020.
- 697 [10] C. Xiao, N. Chen, C. Hu, *et al.*, "A spatiotemporal deep learning model for sea surface  
698 temperature field prediction using time-series satellite data," *Environmental Modelling &  
699 Software*, vol. 120, p. 104502, 2019.
- 700 [11] A. Ducournau and R. Fablet, "Deep learning for ocean remote sensing: An application  
701 of convolutional neural networks for super-resolution on satellite-derived sst data," in  
702 *2016 9th IAPR Workshop on Pattern Recognition in Remote Sensing (PRRS)*, IEEE, 2016,  
703 pp. 1–6.
- 704 [12] M. Tang, Y. Liu, and L. J. Durlofsky, "A deep-learning-based surrogate model for data  
705 assimilation in dynamic subsurface flow problems," *Journal of Computational Physics*,  
706 vol. 413, p. 109456, 2020.

- 707 [13] G.-Q. Jiang, J. Xu, and J. Wei, "A deep learning algorithm of neural network for the  
708 parameterization of typhoon-ocean feedback in typhoon forecast models," *Geophysical*  
709 *Research Letters*, vol. 45, no. 8, pp. 3706–3716, 2018.
- 710 [14] Y. Zhu, G. Cao, Y. Wang, *et al.*, "Variability of the deep south china sea circulation derived  
711 from hycom reanalysis data," *Acta Oceanologica Sinica*, vol. 41, no. 7, pp. 54–64, 2022.
- 712 [15] B. Kesavakumar, P. Shanmugam, and R. Venkatesan, "Enhanced sea surface salinity  
713 estimates using machine-learning algorithm with smap and high-resolution buoy data,"  
714 *IEEE Access*, vol. 10, pp. 74 304–74 317, 2022.
- 715 [16] D.-H. Kim and H. M. Kim, "Deep learning for downward longwave radiative flux forecasts  
716 in the arctic," *Expert Systems with Applications*, vol. 210, p. 118 547, 2022.
- 717 [17] R. Zhang, Q. Liu, R. Hang, and G. Liu, "Predicting tropical cyclogenesis using a deep  
718 learning method from gridded satellite and era5 reanalysis data in the western north pacific  
719 basin," *IEEE Transactions on Geoscience and Remote Sensing*, vol. 60, pp. 1–10, 2021.
- 720 [18] S.-W. Kim, J. A. Melby, N. C. Nadal-Caraballo, and J. Ratcliff, "A time-dependent  
721 surrogate model for storm surge prediction based on an artificial neural network using  
722 high-fidelity synthetic hurricane modeling," *Natural Hazards*, vol. 76, no. 1, pp. 565–585,  
723 2015.
- 724 [19] L. Huang, Y. Jing, H. Chen, L. Zhang, and Y. Liu, "A regional wind wave prediction  
725 surrogate model based on cnn deep learning network," *Applied Ocean Research*, vol. 126,  
726 p. 103 287, 2022.
- 727 [20] G. Qiu, Y. Liu, J. Zhao, *et al.*, "Analytic deep learning-based surrogate model for op-  
728 erational planning with dynamic ttc constraints," *IEEE Transactions on Power Systems*,  
729 vol. 36, no. 4, pp. 3507–3519, 2021. DOI: 10.1109/TPWRS.2020.3041866.
- 730 [21] S. C. James, Y. Zhang, and F. O'Donncha, "A machine learning framework to forecast  
731 wave conditions," *Coastal Engineering*, vol. 137, pp. 1–10, 2018.
- 732 [22] P. Pokhrel, M. Abdelguerfi, and E. Ioup, "A machine learning and data assimilation  
733 forecasting framework for surface waves," *Quarterly Journal of the Royal Meteorological*  
734 *Society*, 2023.
- 735 [23] M. Raissi, P. Perdikaris, and G. E. Karniadakis, "Physics-informed neural networks: A  
736 deep learning framework for solving forward and inverse problems involving nonlinear  
737 partial differential equations," *Journal of Computational physics*, vol. 378, pp. 686–707,  
738 2019.

- 739 [24] T. de Wolff, H. Carrillo, L. Marti, and N. Sanchez-Pi, "Towards optimally weighted  
740 physics-informed neural networks in ocean modelling," *arXiv preprint arXiv:2106.08747*,  
741 2021.
- 742 [25] C. Dong, G. Xu, G. Han, B. J. Bethel, W. Xie, and S. Zhou, "Recent developments  
743 in artificial intelligence in oceanography," *Ocean-Land-Atmosphere Research*, vol. 2022,  
744 2022.
- 745 [26] M. A. Nabian and H. Meidani, "Physics-informed regularization of deep neural networks,"  
746 *arXiv preprint arXiv:1810.05547*, 2018.
- 747 [27] J. Tu, C. Liu, and P. Qi, "Physics-informed neural network integrating pointnet-based  
748 adaptive refinement for investigating crack propagation in industrial applications," *IEEE*  
749 *Transactions on Industrial Informatics*, vol. 19, no. 2, pp. 2210–2218, 2022.
- 750 [28] H. Sun, L. Peng, J. Lin, S. Wang, W. Zhao, and S. Huang, "Microcrack defect quan-  
751 tification using a focusing high-order sh guided wave emat: The physics-informed deep  
752 neural network gwnet," *IEEE Transactions on Industrial Informatics*, vol. 18, no. 5,  
753 pp. 3235–3247, 2021.
- 754 [29] H. Sun, L. Peng, S. Huang, *et al.*, "Development of a physics-informed doubly fed  
755 cross-residual deep neural network for high-precision magnetic flux leakage defect size  
756 estimation," *IEEE Transactions on Industrial Informatics*, vol. 18, no. 3, pp. 1629–1640,  
757 2021.
- 758 [30] J. Zhao, W. Li, X. Yuan, *et al.*, "An end-to-end physics-informed neural network for defect  
759 identification and 3-d reconstruction using rotating alternating current field measurement,"  
760 *IEEE Transactions on Industrial Informatics*, pp. 1–10, 2022. DOI: 10.1109/TII.2022.  
761 3217820.
- 762 [31] G. Huang, Z. Zhou, F. Wu, and W. Hua, "Physics-informed time-aware neural networks  
763 for industrial nonintrusive load monitoring," *IEEE Transactions on Industrial Informatics*,  
764 2022.
- 765 [32] J. Rice, W. Xu, and A. August, "Analyzing koopman approaches to physics-informed ma-  
766 chine learning for long-term sea-surface temperature forecasting," *arXiv preprint arXiv:2010.00399*,  
767 2020.
- 768 [33] S. Yuan, X. Feng, B. Mu, B. Qin, X. Wang, and Y. Chen, "A generative adversarial  
769 network-based unified model integrating bias correction and downscaling for global sst,"  
770 *Atmospheric and Oceanic Science Letters*, p. 100407, 2023.

- 771 [34] T. Yuan, J. Zhu, W. Wang, *et al.*, “A space-time partial differential equation based physics-  
772 guided neural network for sea surface temperature prediction,” *Remote Sensing*, vol. 15,  
773 no. 14, p. 3498, 2023.
- 774 [35] G. E. Karniadakis, I. G. Kevrekidis, L. Lu, P. Perdikaris, S. Wang, and L. Yang, “Physics-  
775 informed machine learning,” *Nature Reviews Physics*, vol. 3, no. 6, pp. 422–440, 2021.
- 776 [36] P. Pokhrel, E. Ioup, J. Simeonov, M. T. Hoque, and M. Abdelguerfi, “A transformer-based  
777 regression scheme for forecasting significant wave heights in oceans,” *IEEE Journal of*  
778 *Oceanic Engineering*, vol. 47, no. 4, pp. 1010–1023, 2022.
- 779 [37] “Ifs documentation cy41r2 - parts 1-5,” in *IFS Documentation CY41R2* (IFS Documenta-  
780 tion 1), IFS Documentation 1. ECMWF, 2016.
- 781 [38] H. H., *Era5 hourly data on single levels from 1959 to present. copernicus climate change*  
782 *service (c3s) climate data store (cds)*. (Accessed on 14-APR-2021), 10.24381/cds.adbb2d47,  
783 2018.
- 784 [39] E. C. Eze and C. R. Chatwin, “Enhanced recurrent neural network for short-term wind  
785 farm power output prediction,” *J. Appl. Sci*, vol. 5, no. 2, pp. 28–35, 2019.
- 786 [40] Y. Yu, H. Yao, and Y. Liu, “Structural dynamics simulation using a novel physics-guided  
787 machine learning method,” *Engineering Applications of Artificial Intelligence*, vol. 96,  
788 p. 103 947, 2020.
- 789 [41] R. Hyndman and G. Athanasopoulos, *Forecasting: principles and practice*, 3rd. Mel-  
790 bourne, Australia: OTexts, 2021, <https://otexts.com/fpp3>.

791

792

793

794

795

796



**Austin B. Schmidt** completed his M.S. degree in computer science in 2021 and is a current awardee of the prestigious SMART scholarship, awarded by the DoD. Mr. Schmidt is currently pursuing a Ph.D. in engineering and applied sciences at the University of New Orleans. Alongside working on degree requirements, he conducts machine learning research at the Canizaro Livingston Gulf States Center for Environmental Informatics (GulfSCEI).

797  
798  
799  
800  
801

**Pujan Pokhrel** received his Ph.D. from the University of New Orleans in engineering and applied sciences and conducts research with the Canizaro Livingston Center for Gulf Informatics. He is currently a Software Engineer at Amazon Web Services. His research interests lie in machine learning, artificial intelligence, computational fluid dynamics, numerical models, and optimization.

802  
803  
804  
805  
806  
807

**Mahdi Abdelguerfi** is currently a professor of computer science at the University of New Orleans (UNO) and the founder and executive director of the interdisciplinary Canizaro-Livingston Gulf States Center for Environmental Informatics (GulfSCEI - pronounced Gulf Sea), whose primary goal is to assist state, federal agencies and non-government organizations solve environmental problems of the coastal margin of the State of Louisiana as well as other Gulf States. Dr. Abdelguerfi is the recipient of the 2022 UNO's Career Research Award. He was awarded the 2003 and 2016 Alan Berman Annual Research Publication Award from the Naval Research Laboratory (NRL) - Department of the Navy for research performed jointly with scientists from NRL. He received the 2016 UNO's Competitive Funding Prize in recognition of outstanding and innovative work in support of UNO's research mission. He was also the recipient of UNO's Early Career Achievement Award for Excellence in Research.

811  
812  
813  
814

**Elias Ioup** received a Ph.D. degree in engineering and applied science from The University of New Orleans. He is currently a Computer Scientist and the Head of the Geospatial Computing Section, U.S. Naval Research Laboratory. His research interests include high-performance geospatial data processing, geospatial and environmental web services, and geospatial data visualization.

815  
816  
817  
818

**David Dobson** received a Ph.D. degree in computational science from The University of Southern Mississippi. He currently leads a cloud computing and security research team at the U.S. Naval Research Laboratory. His research interests include machine learning on big data and cloud computing security.

819

## APPENDIX

820  
821

124 selected buoy observations from the NOAA archive for potential inclusion into train, validation, and test datasets. The numbers selected into each set are displayed in VI.

822  
823  
824  
825  
826  
827  
828  
829

- 51001, 41002, 41004, 41008, 41009, 41010, 41013, 41025, 41040, 41041, 41043, 41044, 41046, 41047, 41048, 41049, 42001, 42002, 42003, 42012, 42019, 42020, 42035, 42036, 42039, 42040, 42055, 42056, 42057, 42058, 42059, 42060, 44005, 44007, 44008, 44009, 44011, 44013, 44014, 44017, 44018, 44020, 44025, 44027, 44065, 44066, 45001, 45002, 45003, 45004, 45005, 55039, 45006, 45007, 45008, 45012, 46001, 46002, 46005, 46006, 46011, 46012, 46013, 46014, 46015, 46022, 46025, 46026, 46027, 46028, 46029, 46035, 46041, 46042, 46047, 46050, 46053, 46054, 46059, 46060, 46061, 46066, 46069, 46070, 46071, 46072, 46073, 46075, 46076, 46077, 46078, 46080, 46081, 46082, 46083, 46084, 46085, 46086, 46087, 46088, 46089, 51000, 51001, 51002, 51003, 51004, 51101, 46221, 46214, 46211, 46224, 46215, 46222, 46213, 46235. 46239, 46240, 46243, 46244, 46232, 44095, 44100, 42099, and 44024.

TABLE VI

NUMBER OF BUOYS DISTRIBUTED INTO EACH DATASET. THERE ARE 127 BUOYS SORTED IN TOTAL.

Subset Contributions by Buoy	Total Number
Total Buoys	124
Train Only	3
Val Only	0
Test Only	1
Train and Test Only	2
Val and Test Only	1
Train/Test/Val Included	86
Not Included At All	31

TABLE VII  
GRU ORIGINAL FORECASTS PER  $\lambda \in [0, 1]$   
RMSE RESULTS OVER 8 FORECAST PERIODS (24 HOURS)

Feature	$\lambda$	1.000	2.000	3.000	4.000	5.000	6.000	7.000	8.000
SST (°C)	0.00	1.117	1.327	1.507	1.663	1.800	1.923	2.035	2.138
	0.10	1.029	1.216	1.370	1.503	1.619	1.724	1.818	1.907
	0.20	1.006	1.178	1.324	1.452	1.567	1.670	1.764	1.850
	0.30	0.986	1.195	1.372	1.529	1.670	1.798	1.918	2.029
	0.40	0.978	1.198	1.387	1.552	1.697	1.826	1.941	2.045
	0.50	0.855	1.038	1.194	1.329	1.449	1.558	1.660	1.757
	0.60	0.828	1.030	1.197	1.342	1.471	1.587	1.691	1.785
	0.70	0.882	1.143	1.370	1.574	1.761	1.932	2.091	2.238
	0.80	0.851	1.067	1.239	1.384	1.508	1.618	1.714	1.801
	0.90	0.781	0.977	1.134	1.262	1.369	1.460	1.539	1.607
1.00	0.887	1.133	1.332	1.497	1.640	1.763	1.872	1.970	
Pressure (hPa)	0.00	6.223	6.663	7.011	7.306	7.569	7.805	8.016	8.202
	0.10	6.240	6.702	7.054	7.344	7.593	7.812	8.004	8.175
	0.20	6.393	7.038	7.536	7.947	8.297	8.599	8.858	9.081
	0.30	6.072	6.643	7.077	7.432	7.736	7.999	8.224	8.419
	0.40	5.746	6.424	6.972	7.437	7.837	8.179	8.467	8.713
	0.50	4.446	5.194	5.753	6.202	6.579	6.898	7.169	7.402
	0.60	2.896	3.632	4.252	4.798	5.285	5.711	6.079	6.401
	0.70	2.343	2.968	3.507	4.013	4.508	4.971	5.383	5.754
	0.80	2.302	2.882	3.378	3.831	4.273	4.692	5.073	5.420
	0.96	2.072	2.657	3.148	3.598	4.037	4.447	4.817	5.154
1.00	2.119	2.832	3.452	4.034	4.600	5.136	5.617	6.051	
Gust (m/s)	0.00	3.044	3.399	3.709	3.975	4.205	4.405	4.580	4.738
	0.10	2.917	3.256	3.554	3.811	4.029	4.212	4.366	4.501
	0.20	2.957	3.312	3.616	3.873	4.090	4.271	4.425	4.560
	0.30	2.809	3.124	3.388	3.606	3.787	3.938	4.065	4.176
	0.40	2.789	3.138	3.438	3.691	3.903	4.077	4.223	4.348
	0.50	2.683	3.076	3.404	3.678	3.906	4.094	4.251	4.387
	0.60	2.538	2.963	3.285	3.541	3.747	3.916	4.059	4.182
	0.70	2.412	2.806	3.107	3.347	3.541	3.700	3.833	3.947
	0.84	2.396	2.782	3.077	3.309	3.497	3.650	3.781	3.894
	0.90	2.415	2.841	3.167	3.429	3.640	3.813	3.958	4.081
1.00	2.378	2.778	3.102	3.368	3.587	3.768	3.923	4.055	

TABLE VIII  
 LSTM ORIGINAL FORECASTS PER  $\lambda \in [0, 1]$   
 RMSE RESULTS OVER 8 FORECAST PERIODS (24 HOURS)

Feature	$\lambda$	1.000	2.000	3.000	4.000	5.000	6.000	7.000	8.000
SST (°C)	0.00	1.089	1.282	1.459	1.616	1.754	1.875	1.983	2.080
	0.10	1.031	1.237	1.418	1.583	1.733	1.867	1.989	2.102
	0.20	1.052	1.241	1.408	1.551	1.672	1.776	1.865	1.943
	0.30	1.120	1.344	1.533	1.694	1.833	1.954	2.060	2.153
	0.40	0.900	1.101	1.272	1.418	1.545	1.658	1.760	1.856
	0.50	0.813	1.005	1.165	1.298	1.415	1.519	1.613	1.700
	0.60	0.788	1.015	1.201	1.360	1.497	1.617	1.723	1.817
	0.68	0.756	0.962	1.127	1.263	1.377	1.475	1.560	1.633
	0.80	0.773	1.001	1.186	1.342	1.478	1.597	1.705	1.805
	0.90	0.798	1.033	1.226	1.388	1.527	1.648	1.753	1.848
1.00	0.850	1.097	1.296	1.462	1.603	1.727	1.835	1.931	
Pressure (hPa)	0.00	6.706	7.270	7.691	8.020	8.288	8.510	8.698	8.858
	0.10	6.371	6.854	7.220	7.517	7.770	7.987	8.176	8.343
	0.20	6.493	7.150	7.666	8.079	8.418	8.700	8.938	9.140
	0.30	6.334	7.070	7.646	8.117	8.517	8.862	9.162	9.424
	0.40	5.788	6.556	7.155	7.653	8.083	8.460	8.791	9.084
	0.50	4.557	5.382	6.017	6.532	6.960	7.316	7.613	7.865
	0.60	2.675	3.410	4.037	4.596	5.101	5.546	5.932	6.269
	0.70	2.472	3.119	3.670	4.163	4.617	5.026	5.385	5.703
	0.82	2.241	2.832	3.319	3.762	4.190	4.594	4.954	5.276
	0.90	2.215	2.817	3.315	3.767	4.205	4.616	4.983	5.310
1.00	2.038	2.656	3.186	3.682	4.183	4.672	5.120	5.524	
Gust (m/s)	0.00	2.944	3.240	3.499	3.717	3.904	4.062	4.197	4.315
	0.10	2.991	3.323	3.602	3.831	4.021	4.179	4.310	4.422
	0.20	2.931	3.260	3.536	3.767	3.962	4.128	4.273	4.402
	0.30	2.836	3.169	3.455	3.697	3.902	4.075	4.225	4.355
	0.40	2.768	3.107	3.399	3.647	3.857	4.034	4.185	4.319
	0.50	2.666	3.018	3.314	3.557	3.756	3.919	4.054	4.168
	0.60	2.535	2.976	3.315	3.584	3.805	3.986	4.136	4.264
	0.72	2.440	2.840	3.148	3.397	3.598	3.762	3.898	4.015
	0.80	2.458	2.914	3.270	3.559	3.798	3.998	4.169	4.318
	0.90	2.413	2.842	3.191	3.478	3.714	3.911	4.077	4.217
1.00	2.386	2.834	3.202	3.514	3.776	3.998	4.186	4.346	

TABLE IX  
 TRANSFORMER ORIGINAL FORECASTS PER  $\lambda \in [0, 1]$   
 RMSE RESULTS OVER 8 FORECAST PERIODS (24 HOURS)

Feature	$\lambda$	1.000	2.000	3.000	4.000	5.000	6.000	7.000	8.000
SST (°C)	0.00	0.918	1.027	1.134	1.240	1.345	1.448	1.547	1.644
	0.10	0.893	1.008	1.121	1.233	1.344	1.451	1.556	1.658
	0.20	0.863	0.985	1.102	1.219	1.334	1.446	1.554	1.659
	0.30	0.829	0.957	1.081	1.204	1.324	1.441	1.555	1.664
	0.40	0.784	0.916	1.044	1.171	1.296	1.418	1.537	1.652
	0.50	0.722	0.852	0.982	1.114	1.244	1.372	1.498	1.620
	0.60	0.668	0.808	0.943	1.078	1.211	1.340	1.464	1.583
	0.70	0.615	0.753	0.885	1.017	1.147	1.273	1.395	1.512
	0.80	0.587	0.724	0.853	0.981	1.107	1.230	1.348	1.463
	0.90	0.572	0.699	0.818	0.936	1.052	1.166	1.276	1.383
1.00	0.568	0.691	0.805	0.918	1.030	1.138	1.243	1.344	
Pressure (hPa)	0.00	6.204	6.447	6.663	6.872	7.076	7.269	7.448	7.613
	0.10	6.060	6.334	6.565	6.783	6.995	7.195	7.379	7.548
	0.20	5.878	6.192	6.441	6.671	6.893	7.100	7.290	7.464
	0.30	5.628	6.005	6.284	6.533	6.767	6.984	7.180	7.358
	0.40	5.240	5.735	6.070	6.353	6.611	6.845	7.053	7.242
	0.50	4.050	4.817	5.326	5.718	6.051	6.338	6.587	6.807
	0.60	2.684	3.421	3.995	4.490	4.934	5.325	5.666	5.966
	0.70	2.231	2.877	3.397	3.865	4.306	4.709	5.063	5.379
	0.80	2.003	2.592	3.069	3.512	3.947	4.354	4.716	5.040
	0.90	1.885	2.446	2.904	3.336	3.775	4.196	4.574	4.914
1.00	1.824	2.391	2.867	3.324	3.799	4.263	4.685	5.070	
Gust (m/s)	0.00	2.901	3.145	3.367	3.567	3.745	3.902	4.042	4.169
	0.10	2.844	3.102	3.332	3.537	3.721	3.882	4.027	4.158
	0.20	2.778	3.052	3.292	3.505	3.696	3.864	4.014	4.150
	0.30	2.699	2.992	3.240	3.459	3.653	3.823	3.974	4.111
	0.40	2.595	2.916	3.177	3.403	3.601	3.774	3.927	4.064
	0.50	2.466	2.827	3.107	3.342	3.545	3.720	3.873	4.009
	0.60	2.321	2.707	3.005	3.251	3.459	3.637	3.791	3.927
	0.70	2.229	2.615	2.917	3.165	3.374	3.551	3.704	3.840
	0.80	2.175	2.555	2.855	3.103	3.311	3.488	3.641	3.777
	0.90	2.150	2.522	2.818	3.064	3.270	3.445	3.596	3.730
1.00	2.138	2.505	2.798	3.042	3.246	3.418	3.567	3.698	

TABLE X  
GRU DIFFERENCED FORECASTS PER  $\lambda \in [0, 1]$   
RMSE RESULTS OVER 8 FORECAST PERIODS (24 HOURS)

Feature	$\lambda$	1.000	2.000	3.000	4.000	5.000	6.000	7.000	8.000
SST (°C)	0.00	0.220	0.339	0.400	0.451	0.493	0.525	0.549	0.569
	0.10	0.221	0.342	0.410	0.467	0.513	0.549	0.575	0.595
	0.20	0.211	0.330	0.384	0.424	0.455	0.479	0.498	0.515
	0.30	0.225	0.349	0.414	0.463	0.501	0.529	0.551	0.569
	0.40	0.218	0.341	0.402	0.448	0.486	0.517	0.543	0.566
	0.50	0.211	0.330	0.382	0.421	0.453	0.480	0.502	0.523
	0.60	0.219	0.339	0.392	0.430	0.458	0.480	0.496	0.510
	0.70	0.218	0.339	0.393	0.432	0.462	0.486	0.505	0.522
	0.80	0.216	0.336	0.389	0.426	0.455	0.479	0.499	0.517
	0.90	0.218	0.337	0.391	0.430	0.461	0.487	0.510	0.532
1.00	0.222	0.340	0.391	0.427	0.455	0.478	0.499	0.518	
Pressure (hPa)	0.00	1.044	1.498	2.003	2.516	3.028	3.504	3.923	4.304
	0.10	1.043	1.474	1.970	2.490	3.010	3.491	3.911	4.291
	0.20	1.059	1.496	1.994	2.514	3.052	3.571	4.049	4.496
	0.30	1.101	1.582	2.094	2.620	3.153	3.635	4.048	4.422
	0.40	1.085	1.536	2.021	2.517	3.016	3.474	3.878	4.249
	0.50	1.149	1.631	2.132	2.647	3.167	3.646	4.069	4.464
	0.58	1.151	1.697	2.214	2.705	3.183	3.622	4.015	4.377
	0.70	1.183	1.699	2.198	2.678	3.162	3.622	4.037	4.429
	0.80	1.224	1.801	2.316	2.796	3.262	3.695	4.078	4.433
	0.90	1.231	1.797	2.297	2.754	3.195	3.613	3.996	4.360
1.00	1.276	1.864	2.365	2.808	3.257	3.720	4.151	4.534	
Gust (m/s)	0.00	2.089	2.668	3.176	3.623	4.006	4.343	4.637	4.901
	0.10	2.122	2.645	3.095	3.481	3.803	4.073	4.298	4.496
	0.20	2.032	2.489	2.880	3.219	3.517	3.786	4.035	4.273
	0.30	2.052	2.511	2.903	3.244	3.535	3.786	4.005	4.201
	0.40	2.101	2.539	2.914	3.228	3.492	3.718	3.912	4.082
	0.50	2.120	2.532	2.883	3.188	3.454	3.687	3.895	4.081
	0.60	2.154	2.541	2.870	3.143	3.369	3.556	3.716	3.856
	0.70	2.222	2.579	2.891	3.158	3.385	3.578	3.747	3.897
	0.80	2.318	2.650	2.947	3.204	3.422	3.605	3.763	3.900
	0.90	2.434	2.759	3.048	3.297	3.508	3.682	3.832	3.962
1.00	2.446	2.756	3.032	3.269	3.470	3.639	3.782	3.908	

TABLE XI  
LSTM DIFFERENCED FORECASTS PER  $\lambda \in [0, 1]$   
RMSE RESULTS OVER 8 FORECAST PERIODS (24 HOURS)

Feature	$\lambda$	1.000	2.000	3.000	4.000	5.000	6.000	7.000	8.000
SST (°C)	0.00	0.214	0.330	0.384	0.424	0.456	0.481	0.501	0.518
	0.10	0.222	0.341	0.405	0.454	0.493	0.525	0.551	0.574
	0.20	0.225	0.356	0.431	0.493	0.546	0.587	0.621	0.652
	0.30	0.220	0.344	0.409	0.458	0.498	0.530	0.557	0.581
	0.40	0.211	0.332	0.389	0.433	0.470	0.501	0.528	0.553
	0.50	0.216	0.336	0.392	0.435	0.474	0.509	0.541	0.570
	0.60	0.222	0.348	0.412	0.459	0.497	0.529	0.557	0.583
	0.70	0.218	0.341	0.397	0.439	0.474	0.505	0.533	0.559
	0.80	0.218	0.338	0.389	0.425	0.452	0.475	0.494	0.511
	0.90	0.215	0.336	0.388	0.424	0.452	0.476	0.495	0.512
1.00	0.230	0.352	0.408	0.448	0.480	0.507	0.531	0.552	
Pressure (hPa)	0.00	1.027	1.463	1.974	2.502	3.035	3.548	4.022	4.461
	0.10	1.065	1.526	2.058	2.612	3.152	3.634	4.038	4.400
	0.20	1.067	1.553	2.068	2.587	3.102	3.567	3.968	4.331
	0.30	1.104	1.579	2.087	2.592	3.085	3.525	3.912	4.272
	0.40	1.097	1.542	2.030	2.542	3.064	3.557	4.015	4.456
	0.50	1.160	1.655	2.147	2.629	3.117	3.576	3.993	4.386
	0.60	1.176	1.710	2.219	2.711	3.195	3.639	4.026	4.387
	0.70	1.180	1.706	2.199	2.666	3.144	3.628	4.088	4.518
	0.76	1.219	1.759	2.262	2.737	3.200	3.635	4.037	4.418
	0.90	1.246	1.795	2.271	2.708	3.159	3.620	4.045	4.434
1.00	1.320	1.913	2.415	2.865	3.322	3.788	4.215	4.603	
Gust (m/s)	0.00	2.059	2.590	3.056	3.469	3.834	4.161	4.463	4.758
	0.10	2.067	2.584	3.023	3.392	3.701	3.957	4.170	4.349
	0.20	2.073	2.561	2.982	3.338	3.633	3.887	4.112	4.313
	0.30	2.077	2.539	2.922	3.240	3.502	3.720	3.906	4.067
	0.40	2.106	2.557	2.968	3.344	3.683	3.993	4.280	4.536
	0.50	2.133	2.584	3.000	3.383	3.729	4.050	4.354	4.638
	0.60	2.197	2.580	2.911	3.198	3.443	3.653	3.840	4.009
	0.70	2.267	2.635	2.955	3.229	3.463	3.660	3.831	3.982
	0.80	2.369	2.703	3.003	3.267	3.492	3.683	3.850	3.998
	0.90	2.393	2.713	3.006	3.260	3.473	3.652	3.806	3.939
1.00	2.470	2.782	3.061	3.299	3.498	3.664	3.806	3.931	

TABLE XII  
 TRANSFORMER DIFFERENCED FORECASTS PER  $\lambda \in [0, 1]$   
 RMSE RESULTS OVER 8 FORECAST PERIODS (24 HOURS)

Feature	$\lambda$	1.000	2.000	3.000	4.000	5.000	6.000	7.000	8.000
SST (°C)	0.00	0.206	0.322	0.380	0.426	0.463	0.494	0.522	0.549
	0.10	0.205	0.321	0.378	0.421	0.456	0.486	0.512	0.539
	0.20	0.204	0.321	0.376	0.417	0.450	0.479	0.504	0.530
	0.30	0.204	0.320	0.374	0.413	0.445	0.472	0.497	0.522
	0.40	0.203	0.320	0.373	0.410	0.441	0.468	0.492	0.516
	0.50	0.202	0.320	0.371	0.408	0.438	0.464	0.488	0.511
	0.60	0.202	0.320	0.370	0.406	0.435	0.461	0.485	0.507
	0.70	0.201	0.319	0.370	0.404	0.433	0.458	0.482	0.504
	0.80	0.201	0.320	0.369	0.404	0.432	0.457	0.479	0.500
	0.90	0.201	0.320	0.369	0.403	0.431	0.456	0.477	0.497
1.00	0.201	0.320	0.370	0.404	0.431	0.455	0.476	0.495	
Pressure (hPa)	0.00	0.933	1.410	1.940	2.470	2.980	3.440	3.847	4.216
	0.10	0.950	1.438	1.966	2.494	3.005	3.463	3.865	4.231
	0.20	0.965	1.465	1.993	2.519	3.029	3.484	3.883	4.246
	0.30	0.984	1.501	2.031	2.553	3.060	3.511	3.904	4.265
	0.40	1.007	1.544	2.079	2.596	3.095	3.541	3.931	4.289
	0.50	1.032	1.594	2.134	2.646	3.136	3.575	3.964	4.320
	0.60	1.059	1.649	2.197	2.700	3.178	3.614	4.003	4.357
	0.70	1.091	1.712	2.269	2.761	3.227	3.662	4.054	4.404
	0.80	1.125	1.783	2.348	2.826	3.281	3.723	4.119	4.461
	0.90	1.160	1.855	2.426	2.889	3.335	3.787	4.184	4.517
1.00	1.197	1.933	2.511	2.958	3.396	3.859	4.256	4.578	
Gust (m/s)	0.00	1.820	2.225	2.573	2.869	3.115	3.319	3.491	3.640
	0.10	1.852	2.251	2.592	2.883	3.125	3.326	3.495	3.642
	0.20	1.885	2.278	2.614	2.901	3.139	3.336	3.503	3.649
	0.30	1.923	2.312	2.643	2.924	3.157	3.351	3.515	3.658
	0.40	1.966	2.351	2.676	2.952	3.181	3.372	3.533	3.673
	0.50	2.012	2.393	2.713	2.984	3.209	3.396	3.554	3.692
	0.60	2.061	2.437	2.751	3.017	3.239	3.422	3.578	3.713
	0.70	2.114	2.484	2.794	3.055	3.272	3.453	3.605	3.738
	0.80	2.171	2.532	2.836	3.093	3.307	3.485	3.635	3.765
	0.90	2.230	2.581	2.880	3.133	3.343	3.518	3.665	3.794
1.00	2.290	2.630	2.923	3.172	3.379	3.552	3.697	3.824	